Advances in Differential Equations and Control Processes 2026, 33(2), 4247.
doi: https://doi.org/10.59400/adecp4247

Article

State-space design and analysis of load frequency control with advanced modeling and controller strategies for single, two, and three-area power systems

Kartik Chandra Patra* , **Asutosh Patnaik**

Department of Electrical Engineering, C.V. Raman Global University, Bhubaneswar 752054, India

*** Corresponding authors:** Kartik Chandra Patra, kcpatra47@rediffmail.com or kcpatra47@gmail.com

CITATION

Patra KC, Patnaik A. State-space design and analysis of load frequency control with advanced modeling and controller strategies for single, two, and three-area power systems. Advances in Differential Equations and Control Processes. 2026; 33(2): 4247. https://doi.org/10.59400/adecp4247

ARTICLE INFO

Received: 10 April 2026
Revised: 18 June 2026
Accepted: 23 June 2026
Available online: 25 June 2026

Abstract: Load Frequency Control (LFC) is a fundamental issue in modern power systems, aimed at maintaining system frequency at its nominal value (50/60 Hz) while ensuring accurate regulation of tie-line power exchanges in interconnected areas. This study develops a comprehensive state-space modeling framework for single-area, two-area, and three-area power systems to support dynamic analysis and controller design. Integral controllers and optimal control strategies based on the Riccati equation—namely, Linear Quadratic Regulator (LQR) and Linear Quadratic Gaussian (LQG)—are implemented to enhance system performance. These controllers effectively minimize frequency and voltage deviations under varying load conditions, thereby improving power quality. To achieve faster and more precise control, a Digital Deadbeat Controller (DDC) is also proposed, ensuring rapid convergence to steady-state conditions. A comparative analysis across different system configurations highlights the steady-state frequency deviations and overall performance improvements. The study also addresses persistent challenges caused by memory-dependent nonlinearities such as backlash/deadband, which induce limit cycle (LC) oscillations and degrade system stability. Backlash nonlinearity, inherent in speed governors used in LFC, plays a significant role in these oscillations. Two methods are proposed to mitigate LC behavior: signal stabilization using deterministic or random inputs. Simulation results obtained using MATLAB/Simulink demonstrate the effectiveness of these approaches. The findings confirm that both DDC and signal stabilization techniques achieve the desired performance ($\Delta f = 0$, $t \to 0$), indicating robust and efficient control suitable for practical power system applications.

Keywords: load frequency control (LFC); signal stabilization; linear quadratic regulator (LQR); digital deadbeat controller (DDC); limit cycles (LC); Linear Quadratic Gaussian (LQG)

1. Introduction

In the present scenario, the deployment of renewable energy sources (RESs) is indispensable and badly demanded; they are now deeply integrated into the power grid and considered as a vital solution [1]. Besides, power system interconnections continue to expand in both scale and complexity, extending from multigrid integration to the development of regional, provincial, and even global energy networks [2,3].

Electrical power cannot be stored/stocked in huge quantities [4]. Which needs production must be equal to consumption again due to their intermittent nature and limited inherent redundancy, RESs likely to introduce instability into the power

system [5].

The frequency of a power system must be preserved at 50 Hz or 60 Hz (nominal value) to ensure reliable and satisfactory operation. Maintaining a stable frequency keeps the speeds of both induction and synchronous machines constant. Deviations beyond acceptable limits can lead to improper functioning of generating units and connected loads, potentially resulting in performance degradation or operational failure [6].

Power system frequency is determined by the real-time balance among generated and demanded active power, and any change in load demand results in two types of deviations: a variation in system frequency within the local area and a change in tie-lines linking interconnected areas. Primary control through the speed governors of individual generating units alone is not sufficient to fully suppress these deviations. To achieve coordinated regulation and optimization objectives.

The AGC system primarily consists of two functions: the automatic voltage regulator (AVR) on LFC. The LFC is responsible for monitoring load demands and regulating frequency deviations, ensuring zero steady-state error (SSE) while maintaining the specified values for power interchange and frequency in interconnected power systems [7–10]. Automatic Generation Control (AGC) performs two primary tasks: (i) regulation of system frequency and maintenance of scheduled inter-area power exchanges, collectively termed LFC, and (ii) optimal allocation of generation among available units to achieve economic operation, known as Economic Dispatch Control (EDC), or tertiary frequency control [11]. In the present work, the emphasis is placed on secondary (supplementary) control. Any variation in generation or load disturbs the active power balance and consequently affects the system frequency, which must remain constant to ensure satisfactory power system operation. Therefore, LFC is implemented for an interconnected system consisting of two or more independently controlled areas. In an interconnected multi-area power system, a disturbance such as a load change in one control area is initially distributed among all participating areas. This results in coordinated generator response, deviations in inter-area tie-line power transfers, and transient declines in system frequency [12]. Several classical control strategies have been employed to implement supplementary (secondary) control to restore frequency to its nominal value in the least time. Among the various control strategies, proportional–integral (PI) controllers [13–15] are extensively employed due to their simplicity and effectiveness. These controllers operate on the load reference input, which regulates the governor speed set-point, thereby facilitating frequency control. This regulation mechanism is also commonly known as LFC.

RESs can introduce instability into the power system, thereby increasing the complexity of control and stabilization [16], may it be LFC or AGC is one of the essential operations that takes place all the time to maintain the power system stable. The modus operandi of LFC is to keep the balance between interconnected areas to control/regulate the power flow in tie-lines connected with the microgrid with RESs under a distributed grid system [17, 18].

The research aims to investigate advancements in LFC and outline the future direction for interconnected multi-area power systems (IMAPSs). The extensive literature survey through 264 nos. of articles have been done [19] and presented the

noteworthy works of many two key articles [20,21] drew our attention.

The integral action is introduced to increase the system type by one, thereby ensuring zero steady-state Δf. The effectiveness of this control strategy depends primarily on the speed regulation constant of the governor and the integral gain (K_i) of the controller. Although this approach is simple to implement, it often results in comparatively large transient frequency deviations. To enhance dynamic performance and achieve improved stability, optimal control techniques based on the state-feedback controller have been idealized [22–24]. However, it has been observed that complete knowledge of system states is often difficult to obtain in practice. To address this limitation, alternative approaches based on adaptive neural networks (ANN) [25, 26] have been explored to enhance dynamic performance. Despite their effectiveness, these methods require extensive training data and significant computational time, which limits their practical applicability.

LFC operates through three levels: primary, secondary, and tertiary control. The primary control mechanism ensures a balance between overall generation and demand, with the turbine governor serving as the main regulator of speed [27,28]. If the primary control system cannot adequately correct frequency deviations, the secondary control system is activated to restore frequency to its nominal value. This system manages power flow among interconnected areas by adjusting the output of individual turbine units [29–31]. When necessary, the tertiary control, also known as the manual frequency restoration reserve, can be engaged by the operator. This level is typically used to replenish the secondary reserve in case of severe generation or load drops [32,33].

Although fuzzy logic–based techniques have also been investigated for LFC in power systems, their implementation remains an area of ongoing research. Sambariya and Nath [34] proposed the use of Δf as inputs to the fuzzy controller, while Indulkar and Raj [35] utilized area control error (ACE) and its rate of change as input variables. Some literature [36, 37] narrated incorporating the deadband/backlash present in the speed governor exhibits LC, leading to poor performance of LFC. To overcome the problem, it is proposed to use DDC with the objective of achieving the best performance/response at steady state in the least time through LFC using a speed governor [38].

2. Controllers used in models of LFC control

2.1. PI controller used for LFC control

Figure 1 represents a single-area interconnected power system used for LFC analysis, where the area is modeled using governor, turbine, and generator-load dynamics represented through transfer functions. The governor block, characterized by gain and time constant parameters, regulates the input to the turbine, which in turn drives the generator and maintains system frequencies. A tie-line is included to represent power exchange among the interconnected areas, and the presence of the $1/R$ block indicates the droop characteristic of the governor. The system operates in a closed-loop configuration where frequency deviation is continuously fed back and corrected. An integral control action, represented by the $1/s$ block, is incorporated to

eliminate steady-state frequency error and improve system stability, while controller gain *K* adjusts the dynamic response. Summing junctions combine signals such as load disturbances, tie-line power deviations, and feedback signals, and the overall system response, particularly frequency deviation over time, is monitored using a scope. This configuration effectively demonstrates the principles of AGC, maintaining frequency stability across interconnected power systems.

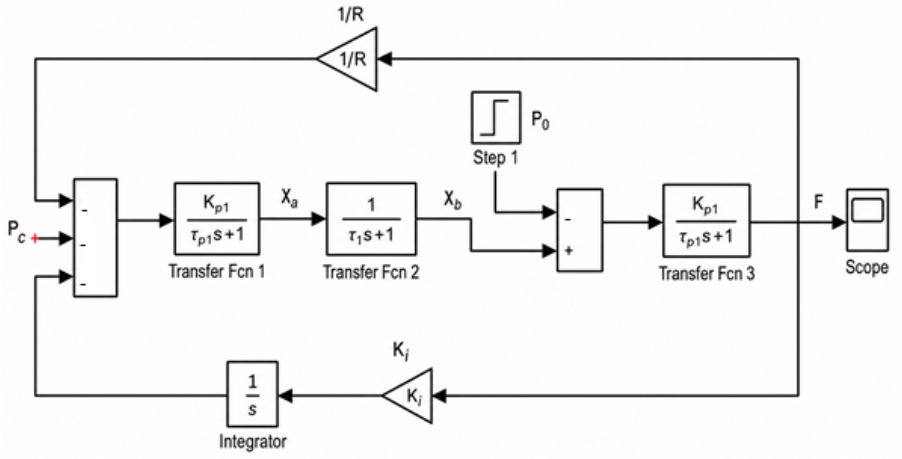

Figure 1. PI control of LFC of a single area system.

- The transfer function $G_1(s) = \frac{K_{p1}}{\tau_{p1}s+1}$ where, K_{p1} is the gain of the first-order process, τ_{p1} is the time constant for the first-order process, and s is the Laplace transform.
- The transfer function $G_2(s) = \frac{1}{\tau_1 s+1}$ where, τ_1 is the time constant of the second first-order lag element.
- The transfer function $G_3(s) = \frac{K_{p3}}{\tau_{p3}s+1}$ where, K_{p3} is the gain of the third process stage, τ_{p3} is the time constant associated with the third stage.

The integrator produces a real-power command signal ΔP_c and is given by

$$\Delta P_c = -K_i \int \Delta f dt = -K_i \int (ACE) dt. \tag{1}$$

Where, P_c = input of speed changer, K_i = integral gain constant.

2.2. Optimal control (LQR) design is used for LFC control against load changes

The application of modern control theory (MCT) facilitates the development of an optimal load frequency control strategy for interconnected two-area power systems [39, 40]. Accordingly, in the MCT approach, single-area optimal LFCs are also developed [40].

In modern control theory, the incremental reference power changes ΔPref1 and ΔPref2 are treated as control inputs, denoted by u1 and u2. In conventional approaches, these control signals are generated by integrating the area control errors (ACEs). However, in modern control practice, u1 and u2 are formulated as linear combinations of the system state in a state-feedback configuration or as linear combinations of selected measurable (or controllable) states in an output-feedback configuration [40,41].

A generalized linear representation (**Figure 2**) of the power system is formulated in the state-space procedure as given below:

$$\frac{dx}{dt} = \text{Ax(t)} + \text{Bu(t)}, \text{ with x(0)} = \text{x}_0, \text{ y} = \text{Cx(t)}, \tag{2}$$

where, x(t) and u(t) are the n and m-dimensional vectors, and y(t) denotes the output vector of the system.

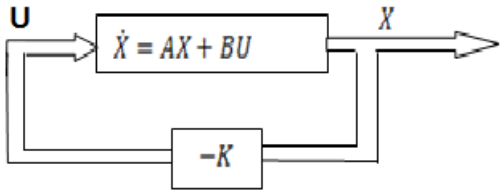

Figure 2. System with state feedback.

The matrices A, B, and C are constant system matrices with dimensions compatible with the state-space formulation. The performance of the system is evaluated using a predefined cost function, which is minimized through the synthesis of an optimal control law.

$$J = \frac{1}{2}\int_0^\infty \left(x^{'}(t)Qx(t) + u^{'}(t)Ru(t)\right) dt. \tag{3}$$

Where the positive semi-definite symmetric weighting matrixes Q, R $\in$ $\mathbb{R}^{n\times n}$ and $\mathbb{R}^{m\times m}$ are the state cost and control cost, respectively.

The optimal control input that minimizes the performance index is expressed in state-feedback form as:

$$u(t) = -Kx(t). \tag{4}$$

Where $K \in R\text{^}(m \times n)$ is the constant state-feedback gain matrix. The gain matrix *K* is obtained by solving the Riccati Equation:

$$A^{'}P + PA - PBR^{-1}B^{'}P + Q = 0, \tag{5}$$

$$K = R^{-1}B^{'}P. \tag{6}$$

An admissible gain matrix *K* must ensure system stability. This requires that all eigenvalues of the matrix *A–BK* must have negative real parts.

In practice, however, measuring and obtaining real-time information for all state variables in large power systems is both difficult and expensive. Typically, only a limited number of state variables, or linear combinations of them, are accessible. Under such conditions, an output feedback controller is employed, which is described as follows.

$$u = -Ky. \tag{7}$$

The linear model described by Equations (1) and (2) can be reorganized into a suitable form for output-feedback controller design.

In case some states are not available, the controllability conditions show that the rank of the controllable matrix is not *n* (the order of the system). In that case, taking into account the observability conditions, the Riccati equation may be considered for

the LQG formulation [42]:

$$A\Sigma \ + \ \Sigma AT \ + \ Q0 \ - \ \Sigma CT \ R_0^{-1} C\Sigma = 0 \text{ and } L = \Sigma C^T R_0^{-1},$$

$$\frac{dx}{dt} = (A - BKC)x = A_C x, \tag{8}$$

$$J = \frac{1}{2}\int_0^\infty \left(x^T Q + C^T K^T RKC\right) x dt. \tag{9}$$

The gain matrix *K* is such that the performance index *J* is minimized, subject to the given dynamical constraints of the system.

$$\frac{dx}{dt} = (A - BKC)x. \tag{10}$$

Whereas dynamic optimization problems can be transformed into their equivalent static optimization problems, which are comparatively easier to solve. With the application of optimization techniques, the following equations are obtained w.r.t optimal gain design.

$$0 = A_c^T P + PA_C - C^T K^T RKC + Q, \tag{11}$$

$$0 = A_c S + SA_c^T + X, \tag{12}$$

$$\mathrm{K} = \mathrm{R}^{-1}\mathrm{B}^{\mathrm{T}}\mathrm{PSC}^{\mathrm{T}}(\mathrm{CSC}^{\mathrm{T}})^{-1}. \tag{13}$$

Where,

$$A_c = A - BKC \text{ and } X = E\left\{x(0)x^T(0)\right\}$$

Assuming that the initial states are uniformly distributed over the surface of the unit sphere, the matrix $X = I$ becomes the identity matrix and is symmetric. In many practical situations, the initial state vector *x(0)* is unknown, and this uncertainty is a common characteristic of output feedback design problems. To address this issue, it is customary to minimize not the performance index itself but rather its expected value [42].

$$X = E\{J\}$$

$$E\{J\} = \frac{1}{2}E\left\{x^T(0)Px(0)\right\} = \frac{1}{2}tr(PX). \tag{14}$$

The optimal cost can be given by,

$$J_0 = tr(PX). \tag{15}$$

To obtain *K* that minimizes J_0, these three coupled equations must be solved simultaneously, typically using an appropriate iterative technique [43].

3. Models for LFC control: Design and analysis in state space

Two mathematical models widely used in power systems, the transfer function and the state space model, are considered to be modern and advanced [44]. A transfer function is used only for linear systems, whereas a state-space model

is used for linear and nonlinear systems. We opted for the state space model for LFC with a speed governor, turbine, and generator in which the governor has inherent backlash-type nonlinearity. Sivanagaraju and Sreenivasan [45] have considered their three models—single-area power system (SAPS), two-area power system (TwAPS), and three-area power system (ThAPS) linearized systems and presented their state-space models. The same has also been presented in Azzam [44] and Kakilli et al. [46]. Since the speed governor has inherent characteristics of backlash nonlinearity, we have considered such nonlinearity in each of their models. The results of simulations are presented in Section 4, where the results of these linear models are along with the results of three other models also considered.

A substantial body of literature has investigated nonlinear characteristics in control systems, including both non-memory nonlinearities and memory-type nonlinearities such as backlash and rectangular hysteresis. These nonlinear effects, when present in third-order or higher-order linear systems, can induce LC oscillations under autonomous conditions [47–52]. It has been widely reported that the occurrence of LCs degrades the performance of LFC. Furthermore, as highlighted in Tsay [53], the mitigation/quenching of sustained oscillations is essential for the effective implementation of LFC. In Sah et al. [54], a schema for power systems and optimized its parameters using the Artificial Gorilla Troops Optimizer (GTO), demonstrating improved frequency regulation and dynamic performance compared with conventional approaches. In Hussain et al. [55], the authors developed a Walrus Optimization Algorithm (WaOA)-based cascade controller for load frequency control of a multi-area power system with renewable energy sources, achieving enhanced frequency stability and superior dynamic performance under varying operating conditions.

3.1. Model with PI control design and analysis in the state space for SAPS

A schematic representation of LFC for a turbo-generator is illustrated in **Figure 3**. In this configuration, a frequency sensing unit detects the frequency deviation Δf and generates a corresponding control signal. The LFC mechanism adjusts the real power exchange over the tie-line, which in turn regulates the position of the prime mover inlet valve [45]. The state space equation of a single area can be developed from **Figure 1** in conjunction with **Figure 3** as:

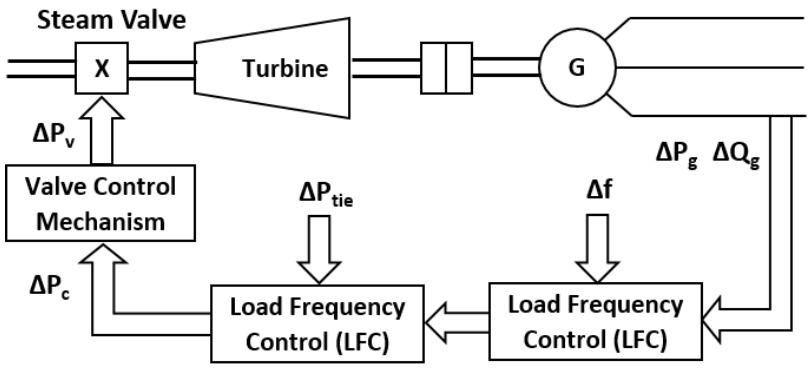

Figure 3. Basic layout of LFC with a PI controller for SAPS.

3.1.1. Unit step response of the SAPS (linearized model) with a PI controller

The linearized dynamic model of a SAPS under PI-based LFC is formulated using small-signal analysis. The system consists of interconnected governor, turbine, and power system blocks, each represented by first-order dynamics. The following equations describe the evolution of frequency deviation, control valve position, and generated power in response to load disturbances

$$\frac{d}{dt}(\Delta f) = \frac{1}{\tau_{ps}}\left[-\Delta f + K_{ps}\Delta P_G - K_{ps}\Delta P_{GD}\right], \tag{16}$$

$$\frac{d}{dt}\left(\Delta X_E\right) = \frac{1}{\tau_{sg}}\left[-\Delta X_E + \Delta P_C - \Delta f/R\right], \tag{17}$$

$$\frac{d}{dt}\left(\Delta P_G\right) = \frac{1}{\tau_t}\left[-\Delta P_G + \Delta X_E\right]. \tag{18}$$

Where, Δf is the frequency deviation, ΔX_E is the governor valve position deviation, and ΔP_G is the turbine output power deviation.

From the above three equations, the state space matrix is obtained as under:

$$\begin{bmatrix}\Delta X_E\\ \Delta P_G\\ \Delta f\end{bmatrix} = \begin{bmatrix}\dot{X}_1\\ \dot{X}_2\\ \dot{X}_3\end{bmatrix} = \begin{bmatrix}-\frac{1}{\tau_{sg}} & 0 & -\frac{1}{R\tau_{sg}}\\ \frac{1}{\tau_t} & -\frac{1}{\tau_t} & 0\\ 0 & \frac{K_{ps}}{\tau_{ps}} & -\frac{1}{\tau_{ps}}\end{bmatrix}\begin{bmatrix}x_1\\ x_2\\ x_3\end{bmatrix} + \begin{bmatrix}\frac{1}{\tau_{sg}}\\ 0\\ 0\end{bmatrix} u + \begin{bmatrix}0\\ 0\\ -\frac{K_{ps}}{\tau_{ps}}\end{bmatrix} p.$$

In the above matrix, *u* is the system input, and *p* is the disturbance.

Figure 4a illustrates a closed-loop LFC system comprising a governor, turbine, and power system dynamics with integral control. The feedback structure regulates frequency deviation Δ*f*, ensuring zero steady-state error and improved dynamic performance. The plot in **Figure 4b** illustrates an underdamped frequency response with initial overshoot and decaying oscillations, eventually reaching steady state at 16 s with a small residual error, indicating stable but moderately damped system behavior.

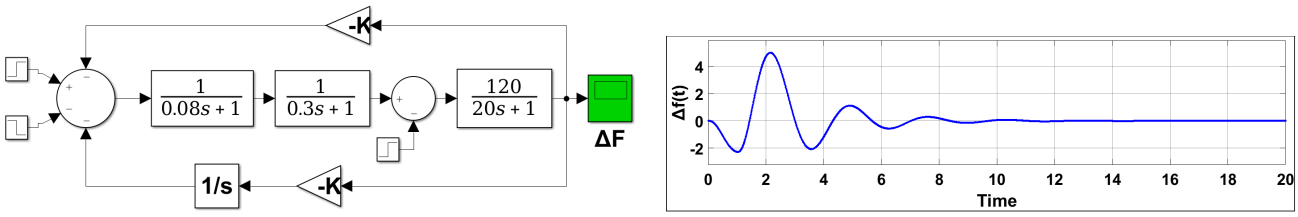

(a) **(b)**

Figure 4. **(a)** Block diagram representation for determination of the unit step response of a SAPS for LFC with a PI controller (Governor without Backlash nonlinearity); **(b)** Frequency deviation in the SAPS for LFC with a PI controller.

3.1.2. Estimation of LC induced by speed governor backlash nonlinearity in SAPS with a PI controller

Figure 5a illustrates a nonlinear LFC system incorporating governor, turbine, and power system dynamics with integral control and a nonlinear element (backlash/ deadband). The feedback loop regulates frequency deviation while capturing practical nonlinear effects that may induce oscillations. The plot in **Figure 5b** illustrates

sustained periodic oscillations in $\Delta f(t)$, confirming the existence of a limit cycle due to system nonlinearities, resulting in degraded frequency regulation and poor dynamic performance.

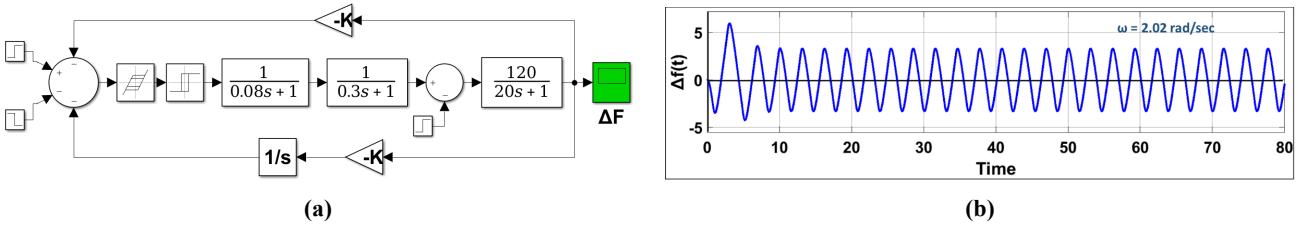

(a) **(b)**

Figure 5. **(a)** Block diagram representation for estimation of LC (incorporating backlash nonlinearity) in speed governor for SAPS with PI controller; **(b)** Frequency deviation in single-area LFC with limit cycle oscillations for SAPS with PI controller.

3.1.3. Signal stabilization by a high-frequency deterministic (at least 10 times of LC frequency) signal for SAPS with a PI controller

Every model presented and examined in Section 3 demonstrates persistent oscillatory behavior, known as LCs, induced by speed governor backlash nonlinearity. These undesired oscillations are successfully quenched/mitigated by applying high-frequency dither inputs, with frequencies chosen to be preferably/approximately 10 times [50, 51] greater than the respective LC frequencies observed in each case. The applied dither signal, whether deterministic or stochastic (e.g., Gaussian), suppresses the limit cycle behavior without significantly altering the overall system dynamics [47–52].

The literature consistently reports that LCs degrade the performance of LFCs. Furthermore, it is emphasized in Tsay [53] that the elimination of sustained oscillations is essential for the reliable and effective operation of LFC.

Figure 6a represents an LFC system with nonlinear effects and deterministic high-frequency signal injection. The dither input mitigates limit cycles, improves damping, and enhances frequency regulation performance by incorporating governor nonlinearities. **Figure 6b** shows the change in frequency (Δf) over time, exhibiting a damped oscillatory behavior where the amplitude of oscillations decreases gradually. Initially, there is a large overshoot followed by oscillations above and below zero, indicating an underdamped response. As time progresses, these oscillations decay steadily, showing that the system is stable and moving toward equilibrium. Around 50–60 s, the response becomes nearly steady with minimal fluctuations, as highlighted in the circled region. The inset graph indicates a higher-frequency oscillation with an angular frequency of approximately 20.3 rad/s. Overall, the system eventually settles at a steady-state condition where Δf approaches zero.

3.1.4. Signal stabilization by a high-frequency random (Gaussian) signal for SAPS with a PI controller

Figure 7a represents a closed-loop control system that begins with a Gaussian noise source (mean = 100, variance = 0.05), which is passed through a low-pass filter to remove high-frequency components. The filtered signal enters a feedback loop containing dynamic elements such as gain blocks and an integrator (1/s), all of which

influence the system's response. Feedback paths with gains regulate the behavior of the system, helping maintain stability. The final output, labeled *Δf*, reflects the combined effect of noise filtering and controlled dynamic response. **Figure 7b** shows the corresponding response of **Figure 7a**.

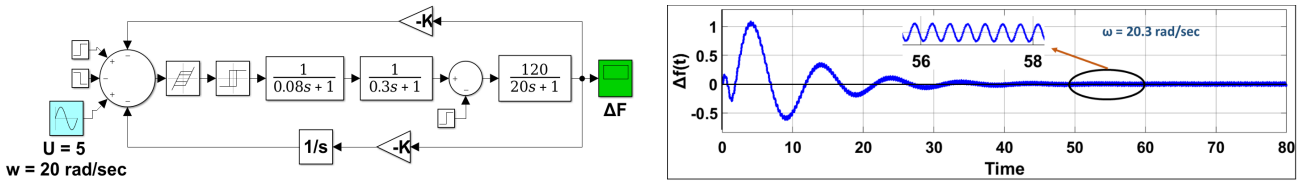

(a) **(b)**

Figure 6. **(a)** Block diagram representation of a SAPS incorporating a proportional–integral (PI) controller, with signal stabilization achieved through a deterministic dither input; **(b)** Frequency deviation in single-area LFC for SAPS with a PI controller for signal stabilization.

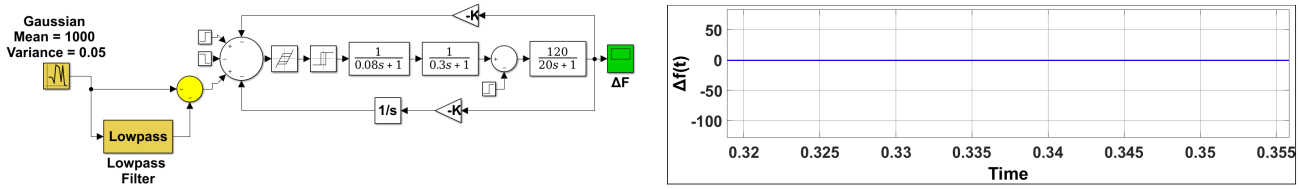

(a) **(b)**

Figure 7. **(a)** Block diagram representation of a SAPS with a PI controller for signal stabilization by a Gaussian signal; **(b)** Signal stabilization by a high-frequency random (Gaussian) signal for a SAPS with a PI controller.

3.2. Model with optimal (LQR) controller: Design and analysis in state space for SAPS

3.2.1. Unit step response of the SAPS (linearized model) with an optimal (LQR) controller

Figure 8a illustrates a closed-loop LFC system comprising a governor, turbine, and power system dynamics with an LQR controller. The feedback structure regulates frequency deviation Δ*f*, ensuring zero steady-state error and improved dynamic performance. The plot in **Figure 8b** illustrates an underdamped frequency response with initial overshoot and decaying oscillations, eventually reaching steady state at t = 15 s with a small residual error, indicating stable but moderately damped system behavior.

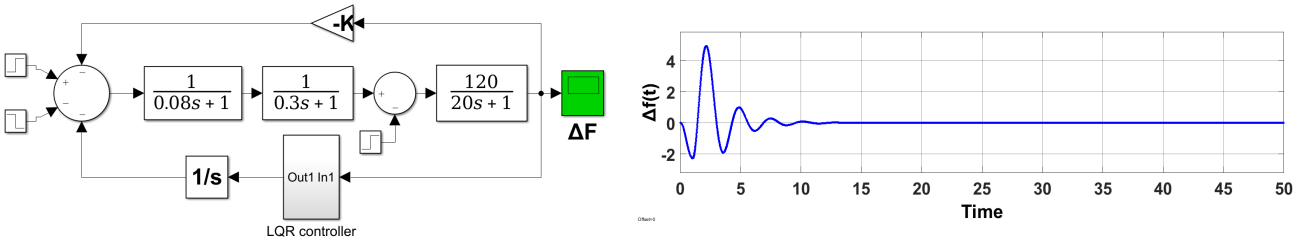

(a) **(b)**

Figure 8. **(a)** Block diagram of LFC SAPS using LQR controller (Governor without Backlash nonlinearity); **(b)** Frequency deviation in SAPS for LFC with LQR controller.

3.2.2. Estimation of LC incorporating backlash nonlinearity in speed governor for SAPS with optimal (LQR) controller

Figure 9a illustrates a nonlinear LFC system incorporating a governor, turbine, and power system dynamics with LQR control and a nonlinear element (backlash/deadband). The feedback loop regulates frequency deviation while capturing practical nonlinear effects that may induce oscillations. The given plot in **Figure 9b** illustrates the frequency deviation Δf of the system over time, where an initial sharp negative dip indicates a sudden disturbance such as a load increase. The system responds quickly, showing a fast transient behavior as the frequency deviation rises toward zero. The response is smooth and well-damped, with no significant oscillations, demonstrating effective control action. The settling time is around 5 s, and the steady-state value approaches zero, indicating that the steady-state error has been eliminated. Overall, the response confirms that the system is stable and properly tuned, with the control mechanism—likely involving LQR control—successfully restoring to the nominal frequency after the disturbance.

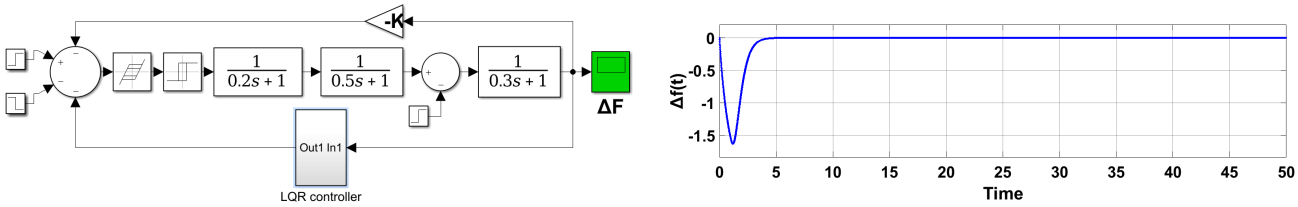

(a) **(b)**

Figure 9. **(a)** Block diagram representation for mitigation of LC induced by backlash nonlinearity, SAPS with LQR controller; **(b)** The frequency deviation Δf of the system over time.

3.2.3. Signal stabilization by a high-frequency deterministic (at least 10 times of LC frequency) signal for SAPS with a LQR controller

The given block diagram in **Figure 10a** represents a LFC system incorporating an LQR controller to regulate frequency deviations in a power system. The input signal, characterized by a stabilizing signal $\omega = 20$ rad/s, is applied to the system, and multiple summing junctions are used to combine control inputs, disturbances, and feedback signals. The given plot in **Figure 10b** shows the frequency deviation Δf response of the system under a sinusoidal disturbance with $\Delta\omega = 20.3$ rad/s. Initially, the system exhibits oscillatory behavior with a noticeable overshoot and undershoot, indicating the effect of the disturbance on system dynamics. These oscillations gradually decrease in amplitude over time, demonstrating a damped response and effective control action. As time progresses, the system stabilizes, and the frequency deviation converges close to zero, indicating minimal steady-state error. The highlighted region toward the later time interval shows that the system maintains a nearly constant value with very small oscillations, confirming steady-state stability. Overall, the response indicates that the controller successfully suppresses oscillations and ensures stable operation of the power system despite periodic disturbances.

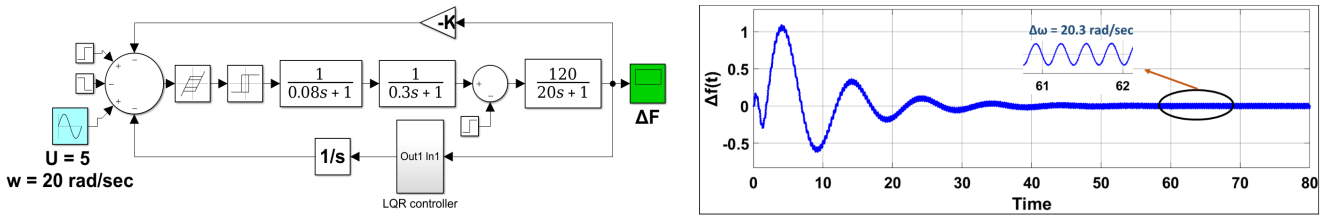

(a) **(b)**

Figure 10. **(a)** Block diagram representation showing signal stabilization by a high-frequency deterministic signal for SAPS with a LQR controller; **(b)** Signal stabilization by a high-frequency deterministic signal for SAPS with a LQR controller.

3.2.4. Signal stabilization by high-frequency random (Gaussian) signal for SAPS with LQR controller

The given block diagram in **Figure 11a** represents a LFC system operating under stochastic disturbances modeled as Gaussian noise with a mean of 300 and a variance of 0.05. The noise signal is first passed through a low-pass filter to smooth out high-frequency components before being applied to the system, ensuring more realistic disturbance characteristics. The graph in **Figure 11b** shows a response curve where the system gradually settles into a steady state after approximately 100 s. Initially, there is a rapid decrease in the value, which then slows as it approaches a stable level. The response does not exhibit any oscillations, indicating a smooth transition without overshooting or fluctuating around the final value. This behavior suggests a well-damped system, and the absence of oscillations can be further ensured or improved through the application of DDC, which helps maintain stability and precise control over the system's performance.

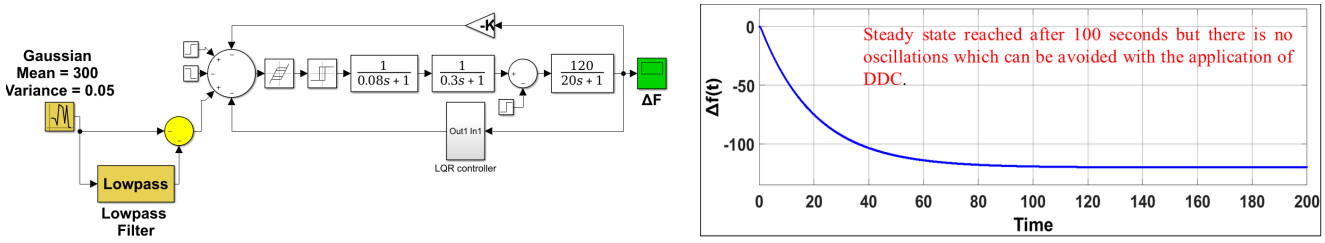

(a) **(b)**

Figure 11. **(a)** Simulink representation of signal stabilization in a standalone power system (SAPS) using a linear quadratic regulator (LQR) controller with high-frequency stochastic (Gaussian) signal injection; **(b)** Signal stabilization by high-frequency random (Gaussian) signal for SAPS with an LQR controller.

3.3. Model with a PI controller: Design and analysis in state space for TwAPS

The dynamic modeling of a TwAPS under LFC is formulated using a linearized state-space approach. The model captures the interactions between two interconnected control areas, each consisting of a governor, a turbine, and power system dynamics. A PI controller is incorporated in each area to regulate Δf and maintain scheduled tie-line power exchange.

The state variables include Δf in both areas, governor valve positions, generated powers, and tie-line power deviations. The coupling between the two areas is

represented through the tie-line power dynamics, which depend on the *Δf* between the areas. The model assumes small perturbations around the nominal operating point, enabling linearization of the system equations. The resulting set of first-order differential equations describes the dynamic response of the interconnected system to load disturbances:

$$\frac{d}{dt}(\Delta f_1) = \frac{1}{\tau_{ps1}}\left[-\Delta f1 + K_{ps1}\Delta P_{G1} - K_{ps1}\Delta P_{D1} - K_{ps1}\Delta P_{TL}\right], \tag{19}$$

$$\frac{d}{dt}(\Delta f_2) = \frac{1}{\tau_{ps2}}\left[-\Delta f2 + K_{ps2}\Delta P_{G2} - K_{ps2}\Delta P_{D2} + K_{ps2}\Delta P_{TL1}\right], \tag{20}$$

$$\frac{d}{dt}(\Delta X_{E1}) = \frac{1}{\tau_{sg1}}\left[-\Delta X_{E1} + \Delta P_{C1} - \Delta f_1/R_1\right], \tag{21}$$

$$\frac{d}{dt}(\Delta X_{E2}) = \frac{1}{\tau_{sg2}}\left[-\Delta X_{E2} + \Delta P_{C2} - \Delta f_2/R_2\right], \tag{22}$$

$$\frac{d}{dt}(\Delta P_{G1}) = \frac{1}{\tau_{t1}}\left[-\Delta P_{G1} + \Delta X_{E1}\right], \tag{23}$$

$$\frac{d}{dt}(\Delta P_{G2}) = \frac{1}{\tau_{t2}}\left[-\Delta P_{G2} + \Delta X_{E2}\right], \tag{24}$$

$$\frac{d}{dt}(\Delta P_{TL1}) = 2\pi T_{12}^0\left[\Delta f_1 - \Delta f_2\right], \tag{25}$$

$$\begin{bmatrix}\Delta X_{E1}\\ \Delta X_{E2}\\ \Delta P_{G1}\\ \Delta P_{G2}\\ \Delta f_1\\ \Delta f_2\\ \Delta P_{TL1}\end{bmatrix} = \begin{bmatrix}\dot{X}_1\\ \dot{X}_2\\ \dot{X}_3\\ \dot{X}_4\\ \dot{X}_5\\ \dot{X}_6\\ \dot{X}_7\end{bmatrix} = \begin{bmatrix} -\frac{1}{\tau_{ps1}} & 0 & 0 & 0 & \frac{K_{ps1}}{\tau_{ps1}} & 0 & -\frac{K_{ps1}}{\tau_{ps1}} \\ 0 & -\frac{1}{\tau_{ps2}} & 0 & 0 & 0 & \frac{K_{ps2}}{\tau_{ps2}} & \frac{K_{ps2}}{\tau_{ps2}} \\ -\frac{1}{R_1\tau_{sg1}} & 0 & -\frac{1}{\tau_{sg1}} & 0 & 0 & 0 & 0 \\ 0 & -\frac{1}{R_2\tau_{sg2}} & 0 & -\frac{1}{\tau_{sg2}} & 0 & 0 & 0 \\ 0 & 0 & \frac{1}{\tau_{t1}} & 0 & -\frac{1}{\tau_{t1}} & 0 & 0 \\ 0 & 0 & 0 & \frac{1}{\tau_{t2}} & 0 & -\frac{1}{\tau_{t2}} & 0 \\ 2\pi T_{12}^0 & -2\pi T_{12}^0 & 0 & 0 & 0 & 0 & 0 \end{bmatrix}\begin{bmatrix}x_1\\ x_2\\ x_3\\ x_4\\ x_5\\ x_6\\ x_7\end{bmatrix} + \begin{bmatrix} 0 & 0 \\ 0 & 0 \\ \frac{1}{\tau_{sg1}} & 0 \\ 0 & \frac{1}{\tau_{sg2}} \\ 0 & 0 \\ 0 & 0 \\ 0 & 0 \end{bmatrix}\begin{bmatrix}u_1\\ u_2\end{bmatrix} + \begin{bmatrix} -\frac{K_{ps1}}{\tau_{ps1}} & 0 \\ 0 & -\frac{K_{ps2}}{\tau_{ps2}} \\ 0 & 0 \\ 0 & 0 \\ 0 & 0 \\ 0 & 0 \end{bmatrix}\begin{bmatrix}p_1\\ p_2\end{bmatrix}.$$

3.3.1. Unit step response of TwAPS (linearized model) with a PI controller

The block diagram in **Figure 12a** represents a controlled dynamic system composed of TwAPS for LFC with a PI controller. The plot in **Figure 12b** shows the system response *Δf(t)* with initial oscillations that gradually decay over time. Both curves converge to a stable steady-state value at 8 s, indicating a damped and well-controlled system response.

3.3.2. Estimation of LC oscillations incorporating backlash nonlinearity and a PI controller in a speed governor for TwAPS

The block diagram in **Figure 13a** represents a controlled dynamic system composed of TwAPS for LFC incorporating backlash nonlinearity and a PI controller in the governor. The plot in **Figure 13b** shows the system response showing the LC.

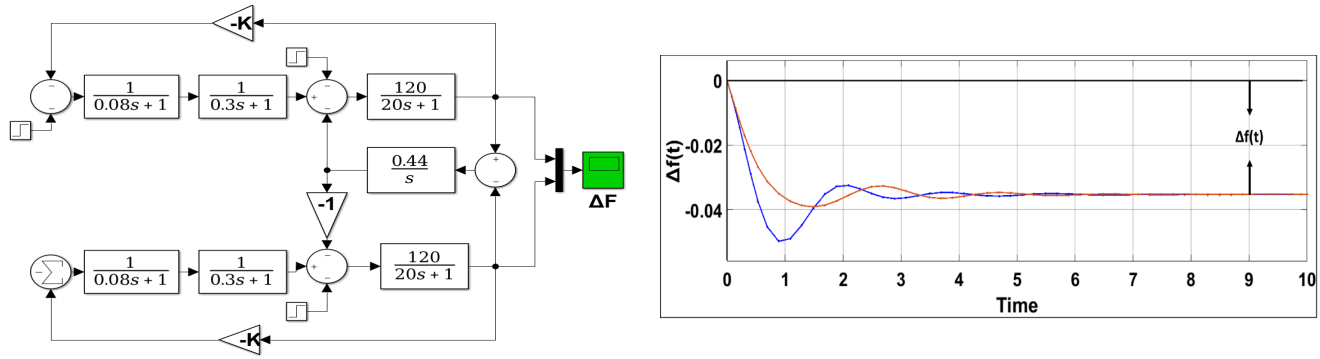

(a) **(b)**

Figure 12. **(a)** Block diagram representation of TwAPS for LFC with a PI controller (Governor without Backlash nonlinearity); **(b)** Dynamic variation of system frequency and tie-line power following a step load change in a TwAPS employing a PI controller.

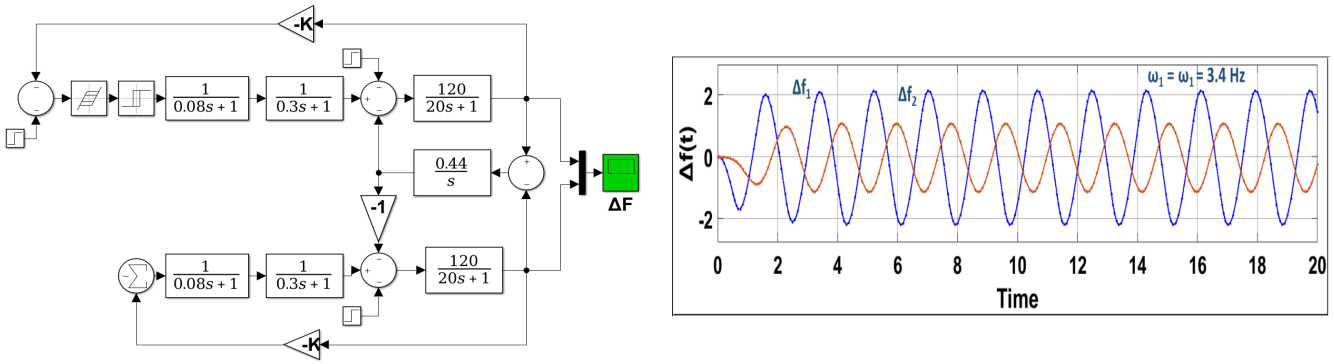

(a) **(b)**

Figure 13. **(a)** Simulink representation of TwAPS with LFC (induced by backlash nonlinearity); **(b)** Estimation of LC incorporating backlash nonlinearity in speed governor for TwAPS with a PI controller.

3.3.3. Signal stabilization by high-frequency deterministic signal for TwAPS with a PI controller

The block diagram in **Figure 14a** represents the signal stabilization composed of TwAPS for LFC incorporating a high-frequency deterministic signal in the governor. The plot in **Figure 14b** shows the system response showing the LC.

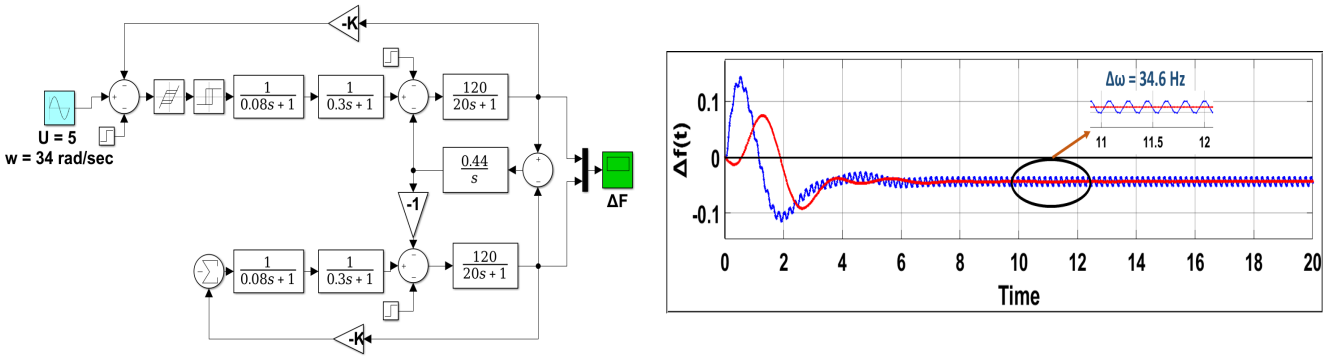

(a) **(b)**

Figure 14. **(a)** Simulink representation presenting signal stabilization by a high-frequency deterministic signal for TwAPS with a PI controller; **(b)** Signal stabilization by a high-frequency deterministic signal for TwAPS with a PI controller.

3.3.4. Signal stabilization by high-frequency random (Gaussian) signal for TwAPS with a PI controller

The block diagram in **Figure 15a** represents a controlled dynamic system composed of TwAPS for LFC incorporating a Gaussian signal and a PI controller in the governor. The plot in **Figure 15b** shows the system response $\Delta f(t)$ with initial oscillations that gradually decay over time. Both curves converge to a stable steady-state value after 8 s, indicating a damped and well-controlled system response.

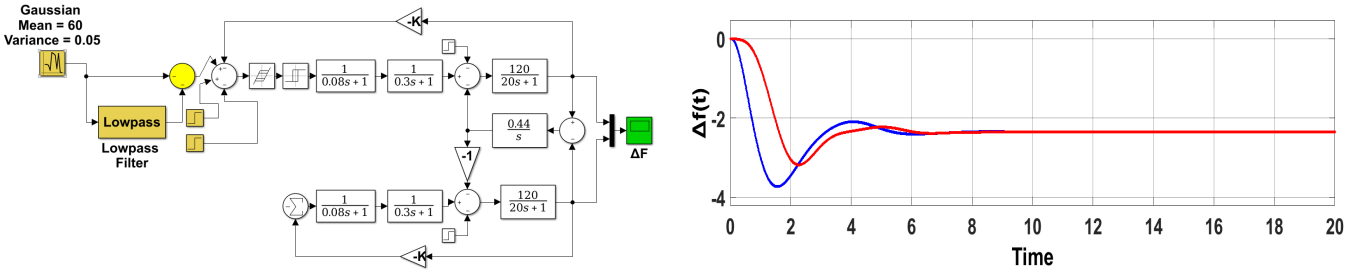

(a) **(b)**

Figure 15. **(a)** Simulink representation presenting signal stabilization induced by a Gaussian signal for TwAPS with a PI controller; **(b)** Signal stabilization by a high-frequency random (Gaussian) signal for TwAPS with a PI controller.

3.4. Model with optimal (LQR) controller: Design and analysis in state space of TwAPS

3.4.1. Unit step response of TwAPS (linearized model) with optimal (LQR) controller

The block diagram in **Figure 16a** represents a controlled dynamic system composed of TwAPS for LFC with an LQR controller. The plot in **Figure 16b** shows the system response $\Delta f(t)$ with initial oscillations that gradually decay over time. Both curves converge to a stable steady-state value after 16 s, indicating a damped and well-controlled system response.

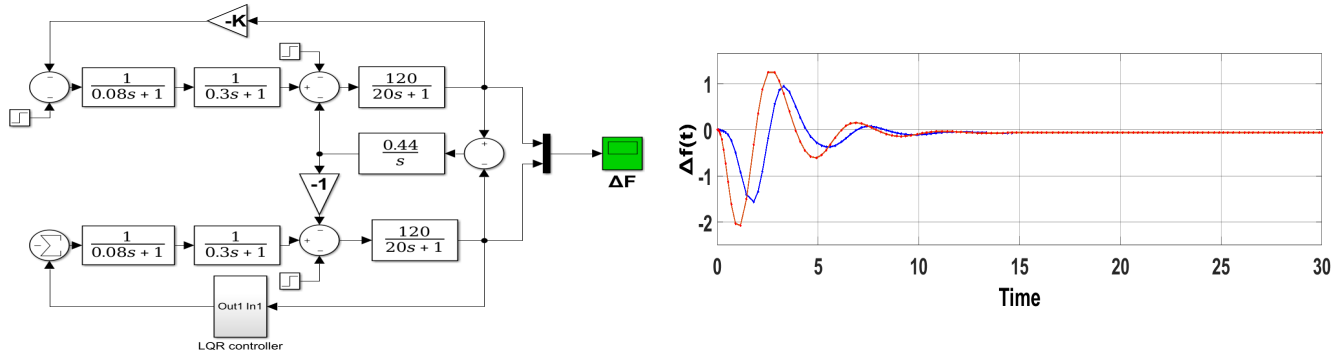

(a) **(b)**

Figure 16. **(a)** Block diagram representation showing the unit-step response of TwAPS (linearized model) with an optimal (LQR) controller (Governor without Backlash nonlinearity); **(b)** Unit-step response of TwAPS (linearized model) with an optimal (LQR) controller.

3.4.2. Estimation of LC oscillations in TwAPS incorporating speed governor backlash nonlinearity under optimal LQR control

Figure 17b shows the system response with the estimation of LC incorporating the backlash nonlinearity in the speed governor for TwAPS with an optimal (LQR) controller.

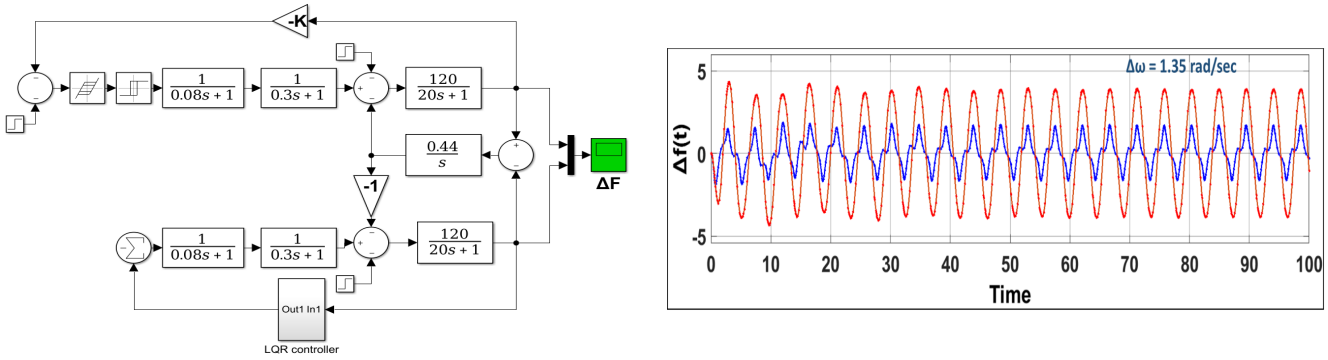

(a) **(b)**

Figure 17. **(a)** Block diagram of LC (induced by backlash nonlinearity) in speed governor for TwAPS with optimal (LQR) controller; **(b)** System response with estimation of LC induced by backlash nonlinearity in speed governor for TwAPS with optimal (LQR) controller.

3.4.3. Signal stabilization by high-frequency deterministic signal for TwAPS with an optimal (LQR) controller

Figure 18a shows signal stabilization by a high-frequency deterministic signal for TwAPS with an optimal (LQR) controller. **Figure 18b** shows the system response to signal stabilization by a high-frequency deterministic signal for TwAPS with an optimal (LQR) controller as in **Figure 18a.**

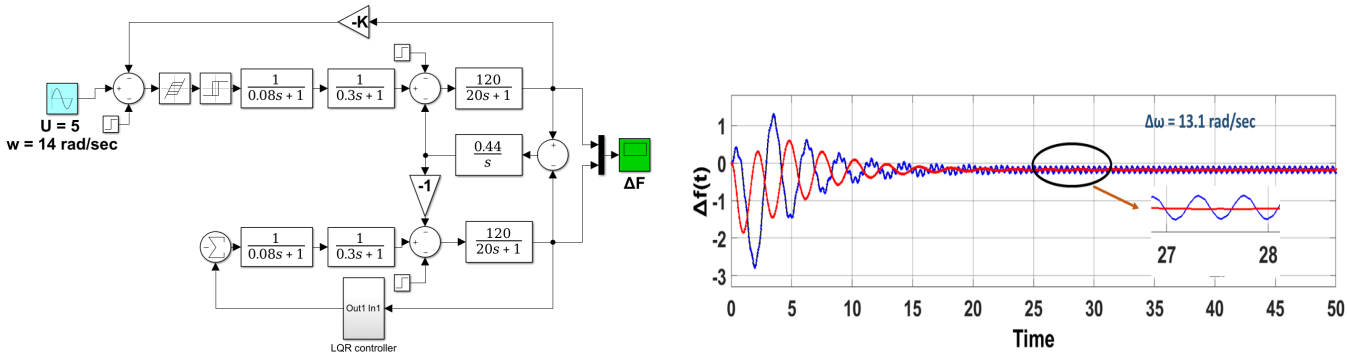

(a) **(b)**

Figure 18. **(a)** Signal stabilization by high-frequency deterministic signal for TwAPS with an optimal (LQR) controller; **(b)** The system response to Signal stabilization by high-frequency deterministic signal for TwAPS with an optimal (LQR) controller.

3.4.4. Signal stabilization by high-frequency random (Gaussian) signal for TwAPS with an optimal (LQR) controller

Figure 19a shows the signal stabilization by Gaussian signals for TwAPS with an optimal (LQR) controller. **Figure 19b** shows the system response to signal stabilization by a Gaussian signal for TwAPS with an optimal (LQR) controller as in **Figure 19a**.

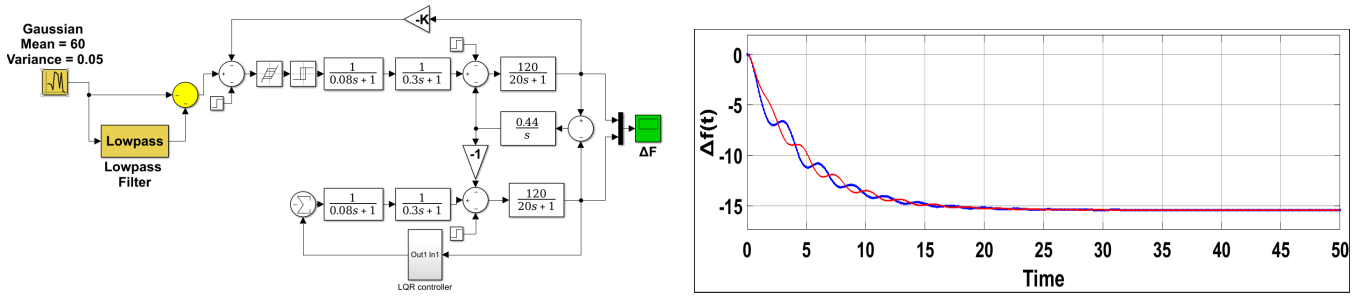

(a) **(b)**

Figure 19. **(a)** Simulink representation presenting signal stabilization induced by a high-frequency Gaussian signal for TwAPS with an optimal (LQR) controller; **(b)** Signal stabilization induced by a high-frequency Gaussian signal for TwAPS with an optimal (LQR) controller.

3.5. Model with a PI controller: Design and analysis in state space for ThAPS

$$
\begin{array}{cccccccccccc}
-\frac{1}{\tau_{ps1}} & 0 & 0 & 0 & 0 & 0 & \frac{K_{ps1}}{\tau_{ps1}} & 0 & 0 & -\frac{K_{ps1}}{\tau_{ps1}} & 0 & 0 \\
0 & -\frac{1}{\tau_{ps2}} & 0 & 0 & 0 & 0 & 0 & \frac{K_{ps1}}{\tau_{ps1}} & 0 & 0 & -\frac{K_{ps1}}{\tau_{ps1}} & 0 \\
0 & 0 & -\frac{1}{\tau_{ps2}} & 0 & 0 & 0 & 0 & 0 & \frac{K_{ps1}}{\tau_{ps1}} & 0 & 0 & -\frac{K_{ps1}}{\tau_{ps1}} \\
-\frac{1}{R_2\tau_{gs1}} & 0 & 0 & -\frac{1}{\tau_{sg1}} & 0 & 0 & 0 & 0 & 0 & 0 & 0 & 0 \\
0 & -\frac{1}{R_2\tau_{g2}} & 0 & 0 & -\frac{1}{\tau_{sg2}} & 0 & 0 & 0 & 0 & 0 & 0 & 0 \\
0 & 0 & -\frac{1}{R_2\tau_{g3}} & 0 & 0 & -\frac{1}{\tau_{sg3}} & 0 & 0 & 0 & 0 & 0 & 0 \\
0 & 0 & 0 & \frac{1}{\tau_{t1}} & 0 & 0 & -\frac{1}{\tau_{t1}} & 0 & 0 & 0 & 0 & 0 \\
0 & 0 & 0 & 0 & \frac{1}{\tau_{t2}} & 0 & 0 & -\frac{1}{\tau_{t2}} & 0 & 0 & 0 & 0 \\
0 & 0 & 0 & 0 & 0 & \frac{1}{\tau_{t3}} & 0 & 0 & -\frac{1}{\tau_{t3}} & 0 & 0 & 0 \\
\pi\left(T_{12}^0+T_{13}^0\right) & -2\pi T_{12}^0 & -2\pi T_{13}^0 & 0 & 0 & 0 & 0 & 0 & 0 & 0 & 0 & 0 \\
2\pi T_{12}^0 & -2\pi\left(T_{12}^0+T_{23}^0\right) & 2\pi T_{23}^0 & 0 & 0 & 0 & 0 & 0 & 0 & 0 & 0 & 0 \\
2\pi T_{13}^0 & 2\pi T_{23}^0 & -2\pi\left(T_{13}^0+T_{23}^0\right) & 0 & 0 & 0 & 0 & 0 & 0 & 0 & 0 & 0
\end{array},
$$

$$\frac{d}{dt}\left(\Delta f_1\right)=\frac{1}{\tau_{ps1}}\left[-\Delta f1+K_{ps1}\Delta P_{G1}-K_{ps1}\Delta P_{D1}-K_{ps1}\Delta P_{TL1}\right], \tag{26}$$

$$\frac{d}{dt}\left(\Delta f_2\right)=\frac{1}{\tau_{ps2}}\left[-\Delta f2+K_{ps2}\Delta P_{G2}-K_{ps2}\Delta P_{D2}+K_{ps2}\Delta P_{TL2}\right], \tag{27}$$

$$\frac{d}{dt}\left(\Delta f_3\right)=\frac{1}{\tau_{ps3}}\left[-\Delta f3+K_{ps3}\Delta P_{G3}-K_{ps3}\Delta P_{D3}+K_{ps3}\Delta P_{TL3}\right], \tag{28}$$

$$\frac{d}{dt}\left(\Delta X_{E1}\right)=\frac{1}{\tau_{sg1}}\left[-\Delta X_{E1}+\Delta P_{C1}-\Delta f_1/R_1\right], \tag{29}$$

$$\frac{d}{dt}\left(\Delta X_{E2}\right)=\frac{1}{\tau_{sg2}}\left[-\Delta X_{E2}+\Delta P_{C2}-\Delta f_2/R_2\right], \tag{30}$$

$$\frac{d}{dt}\left(\Delta X_{E3}\right)=\frac{1}{\tau_{sg3}}\left[-\Delta X_{E3}+\Delta P_{C3}-\Delta f_3/R_3\right], \tag{31}$$

$$\frac{d}{dt}\left(\Delta P_{G1}\right)=\frac{1}{\tau_{t1}}\left[-\Delta P_{G1}+\Delta X_{E1}\right], \tag{32}$$

$$\frac{d}{dt}\left(\Delta P_{G2}\right)=\frac{1}{\tau_{t2}}\left[-\Delta P_{G2}+\Delta X_{E2}\right], \tag{33}$$

$$\frac{d}{dt}\left(\Delta P_{G3}\right)=\frac{1}{\tau_{t3}}\left[-\Delta P_{G3}+\Delta X_{E3}\right], \tag{34}$$

$$\frac{d}{dt}\left(\Delta P_{TL1}\right)=2\pi T_{12}^{0}\left[\Delta f_1-\Delta f_2\right]+2\pi T_{13}^{0}\left[\Delta f_1-\Delta f_3\right], \tag{35}$$

$$\frac{d}{dt}\left(\Delta P_{TL2}\right)=2\pi T_{12}^{0}\left[\Delta f_1-\Delta f_2\right]+2\pi T_{23}^{0}\left[\Delta f_2-\Delta f_3\right], \tag{36}$$

$$\frac{d}{dt}\left(\Delta P_{TL3}\right)=2\pi T_{13}^{0}\left[\Delta f_1-\Delta f_3\right]+2\pi T_{23}^{0}\left[\Delta f_2-\Delta f_3\right], \tag{37}$$

$$\begin{bmatrix}\Delta X_{E1}\\ \Delta X_{E2}\\ \Delta X_{E3}\\ \Delta P_{G1}\\ \Delta P_{G2}\\ \Delta P_{G3}\\ \Delta f_1\\ \Delta f_2\\ \Delta f_3\\ \Delta P_{TL1}\\ \Delta P_{TL2}\\ \Delta P_{TL3}\end{bmatrix}=\begin{bmatrix}\dot{X}_1\\ \dot{X}_2\\ \dot{X}_3\\ \dot{X}_4\\ \dot{X}_5\\ \dot{X}_6\\ \dot{X}_7\\ X_8\\ \dot{X}_9\\ X_{10}\\ \dot{X}_{11}\\ X_{12}\end{bmatrix}=\begin{bmatrix}x_1\\ x_2\\ x_3\\ x_4\\ x_5\\ x_6\\ x_7\\ x_8\\ x_9\\ x_{10}\\ x_{11}\\ x_{12}\end{bmatrix}+\begin{bmatrix}0 & 0 & 0\\ 0 & 0 & 0\\ 0 & 0 & 0\\ \frac{1}{\tau_{sg1}} & \frac{1}{\tau_{sg2}} & 0\\ 0 & 0 & \frac{1}{\tau_{sg3}}\\ 0 & 0 & 0\\ 0 & 0 & 0\\ 0 & 0 & 0\\ 0 & 0 & 0\end{bmatrix}\begin{bmatrix}u_1\\ u_2\\ u_3\end{bmatrix}+\begin{bmatrix}-\frac{K_{ps1}}{\tau_{ps1}} & 0 & 0\\ 0 & -\frac{K_{ps2}}{\tau_{ps2}} & 0\\ 0 & 0 & -\frac{K_{ps3}}{\tau_{ps3}}\\ 0 & 0 & 0\\ 0 & 0 & 0\\ 0 & 0 & 0\\ 0 & 0 & 0\\ 0 & 0 & 0\\ 0 & 0 & 0\\ 0 & 0 & 0\end{bmatrix}\begin{bmatrix}p_1\\ p_2\\ p_3\end{bmatrix}.$$

3.5.1. Unit step response of ThAPS (linearized model) with PI controller

Figure 20a shows the block diagram representation for the unit step response of ThAPS (linearized model) with a PI controller. **Figure 20b** shows the unit step response of ThAPS with a PI controller as in **Figure 20a**, where the steady state is reached at 30 s.

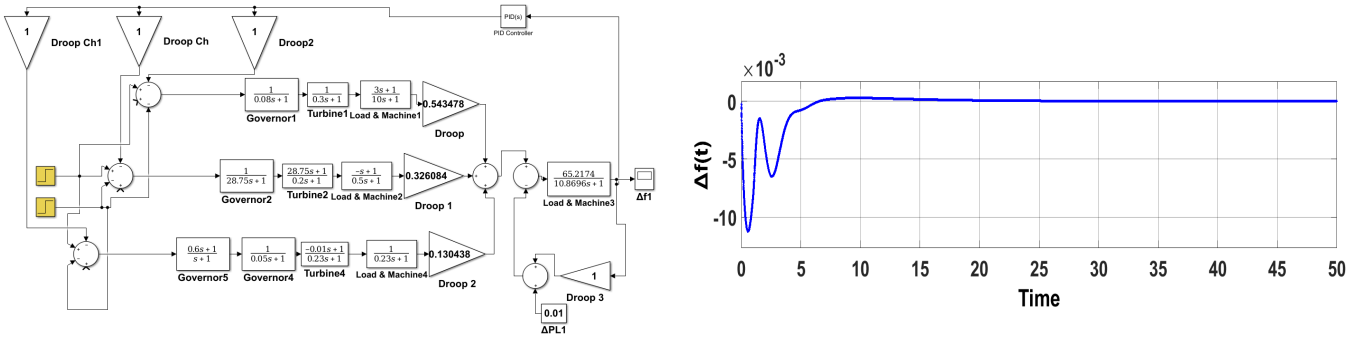

(a) **(b)**

Figure 20. **(a)** Block diagram representation for the unit-step response of ThAPS (linearized model) with a PI controller (Governor without Backlash nonlinearity); **(b)** Unit-step response of ThAPS (linearized model) with a PI controller.

3.5.2. Estimation of LC oscillations in ThAPS incorporating speed governor backlash nonlinearity under a PI controller

Figure 21a shows the Simulink representation showing the estimation of LC in the presence of backlash nonlinearity in the speed governor for ThAPS with a

PI controller. **Figure 21b** shows the system response and the estimation of LC oscillations incorporating backlash nonlinearity in the speed governor for ThAPS with a PI controller.

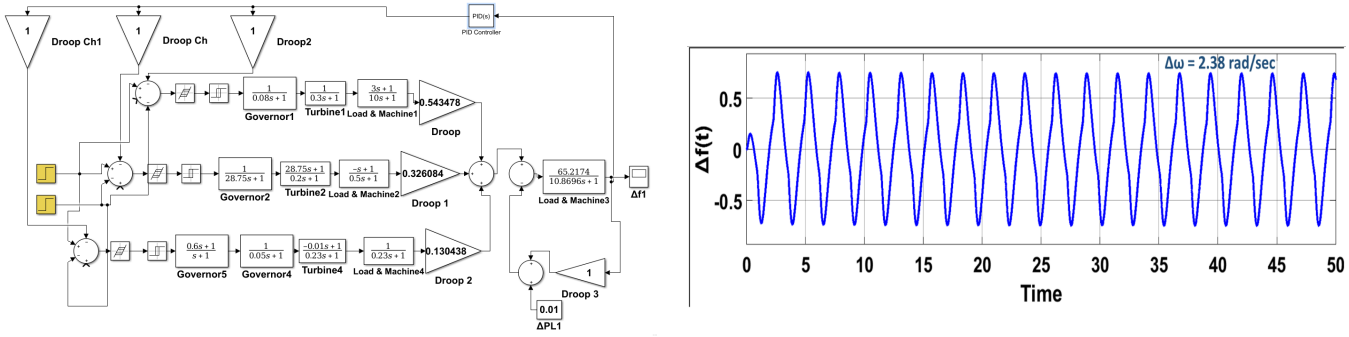

(a) **(b)**

Figure 21. **(a)** Block diagram representation showing the estimation of LC (induced by backlash nonlinearity) in the speed governor for ThAPS with a PI controller; **(b)** Estimation of LC oscillations incorporating backlash nonlinearity in the speed governor for ThAPS with a PI controller.

3.5.3. Signal stabilization by high-frequency deterministic signal for ThAPS with a PI controller

Figure 22a represents the Simulink, presenting the signal stabilization by a high-frequency deterministic signal for ThAPS with a PI controller. **Figure 22b** shows the system response of ThAPS with a PI controller for ThAPS as in **Figure 22a**.

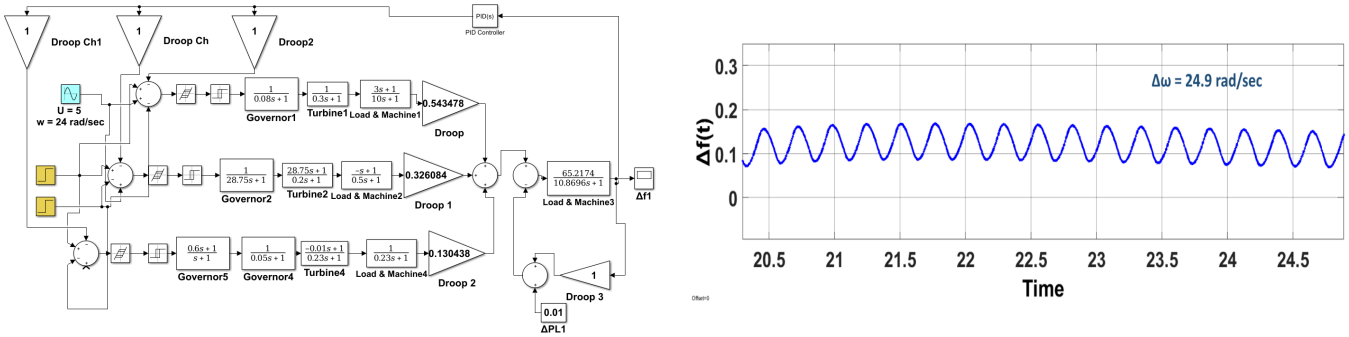

(a) **(b)**

Figure 22. **(a)** Simulink representation presenting signal stabilization by a high-frequency deterministic signal for ThAPS with a PI controller; **(b)** Signal stabilization by a high-frequency deterministic signal for ThAPS with a PI controller.

3.5.4. Signal stabilization by high-frequency random (Gaussian) signal for ThAPS with a PI controller

Figure 23a shows the Simulink representation presenting signal stabilization by a high-frequency Gaussian signal for ThAPS with a PI controller. **Figure 23b** represents the system response of **Figure 23a,** which shows the signal stabilization by a high-frequency random (Gaussian) signal for ThAPS with a PI controller.

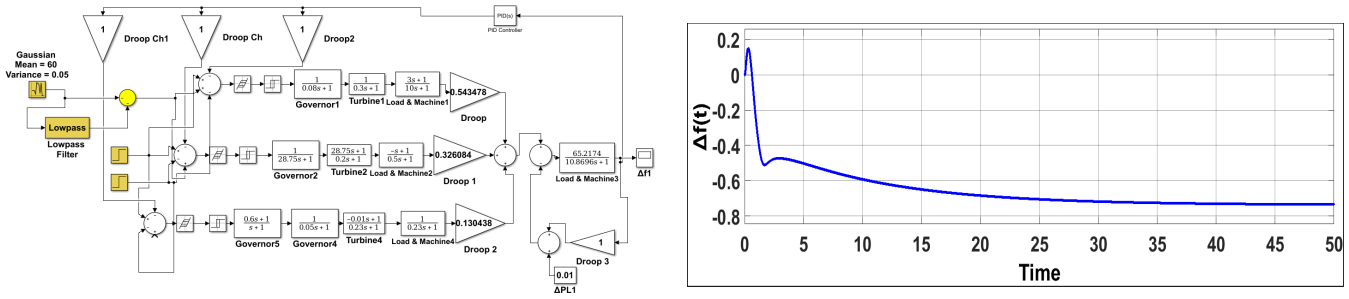

(a) **(b)**

Figure 23. **(a)** Simulink representation presenting signal stabilization by a high-frequency Gaussian signal for ThAPS with a PI controller; **(b)** Signal stabilization by a high-frequency random (Gaussian) signal for ThAPS with a PI controller.

3.6. Model with optimal (LQR) controller: Design and analysis in state space of ThAPS

3.6.1. Unit step response of ThAPS (linearized model) with optimal (LQR) controller

Figure 24a represents the block diagram for the unit step response of ThAPS (linearized model) with an optimal (LQR) controller. **Figure 24b** shows the system response of **Figure 24a,** depicting the unit-step response of ThAPS (linearized model) with an optimal (LQR) controller reaching the steady state at 15 s.

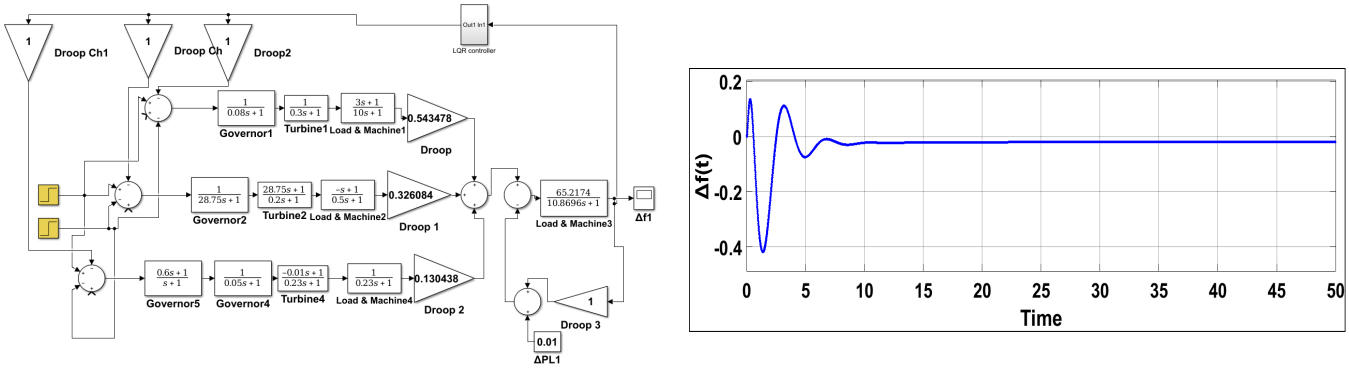

(a) **(b)**

Figure 24. **(a)** Block diagram representation for the unit-step response of ThAPS (linearized model) with an optimal (LQR) controller (Governor without Backlash nonlinearity); **(b)** Unit-step response of ThAPS (linearized model) with an optimal (LQR) controller.

3.6.2. Estimation of LC oscillations incorporating backlash nonlinearity in a speed governor for ThAPS with an optimal (LQR) controller

Figure 25a shows the block diagram representation for estimation of LC oscillations incorporating backlash nonlinearity in the speed governor for ThAPS with an optimal (LQR) controller. **Figure 25b** shows the system response of **Figure 25a** and the estimation of LC oscillations incorporating backlash nonlinearity in the speed governor for ThAPS with an optimal (LQR) controller.

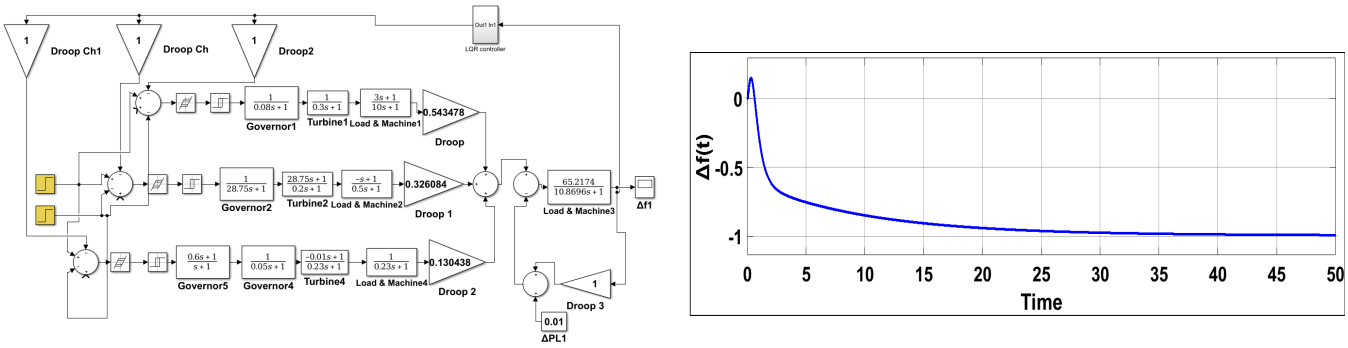

(a) **(b)**

Figure 25. **(a)** Block diagram representation for estimation of LC oscillations (incorporating backlash nonlinearity) in the speed governor for ThAPS with an optimal (LQR) controller; **(b)** Estimation of LC oscillations incorporating backlash nonlinearity in the speed governor for ThAPS with an optimal (LQR) controller.

3.6.3. Signal stabilization by high-frequency deterministic signal for ThAPS with LQR controller

Figure 26a shows the block diagram representation showing signal stabilization by a high-frequency deterministic signal [50, 51] for ThAPS with a LQR controller. **Figure 26b** shows the system response of **Figure 26a** and signal stabilization by a high-frequency deterministic signal (at least 10 times of LC frequency) [50, 51] for ThAPS with a LQR controller.

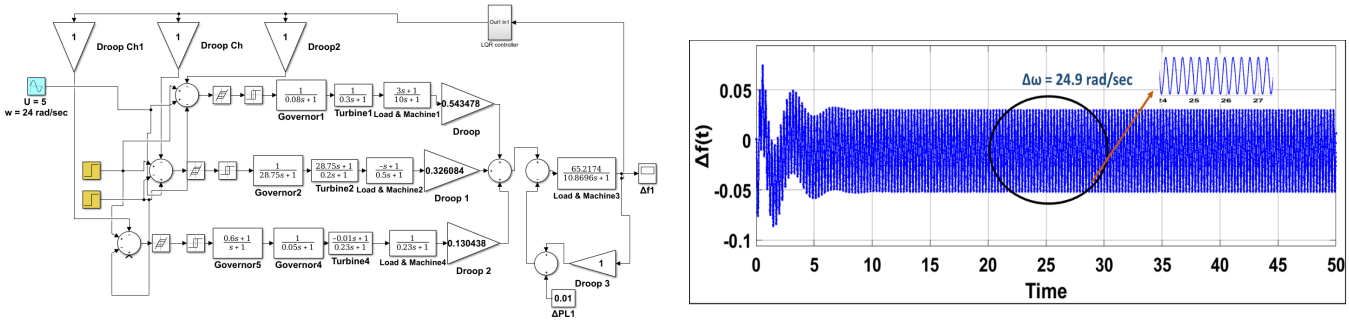

(a) **(b)**

Figure 26. **(a)** Block diagram representation showing signal stabilization by high-frequency deterministic (at least 10 times of LC frequency) signal [50,51] for ThAPS with LQR controller; **(b)** Signal stabilization by high-frequency deterministic (at least 10 times of LC frequency) signal [50,51] for ThAPS with LQR controller.

3.6.4. Signal stabilization by high-frequency random (Gaussian) signal for ThAPS with LQR controller

Figure 27a shows the Simulink representation presenting signal stabilization by a high-frequency Gaussian signal for ThAPS with a LQR controller. **Figure 27b** shows the system response of **Figure 27a** and the signal stabilization by a high-frequency random (Gaussian) signal for ThAPS with a LQR controller.

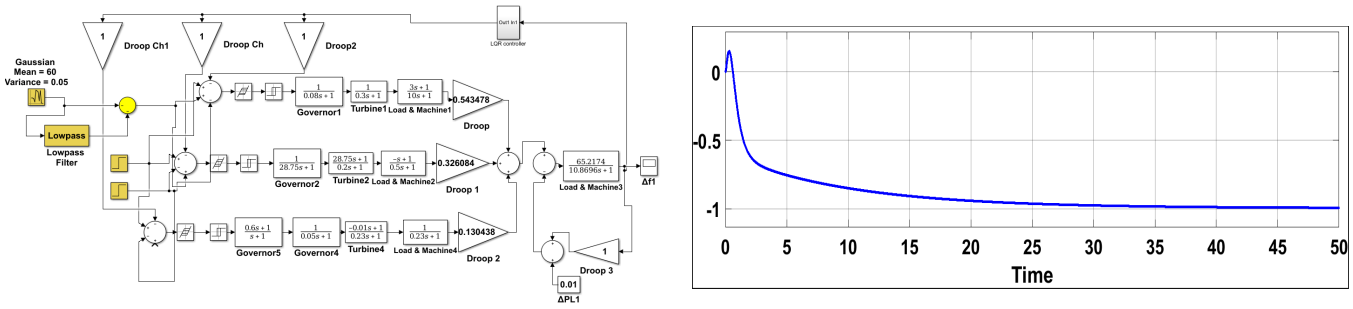

(a) **(b)**

Figure 27. **(a)** Block diagram for signal stabilization by high-frequency random (Gaussian) signal for ThAPS with LQR controller; **(b)** Signal stabilization by high-frequency random (Gaussian) signal for ThAPS with LQR controller.

3.7. Application of digital deadbeat controller (DDC)

"Control systems are often designed with the objective that the output response should reach the desired reference value as quickly as possible and without any overshoot. This type of response is generally referred to as a "deadbeat response" [56].

Deadbeat control relies on a reliable discrete-time representation and often results in aggressive control action. However, practical implementation issues— namely, sampling delays and quantization errors, and actuator saturation—are not addressed in the manuscript. A deadbeat response is defined as a system output that reaches the desired reference value in the minimum number of sampling intervals without overshoot [56], as illustrated in **Figure 28**.

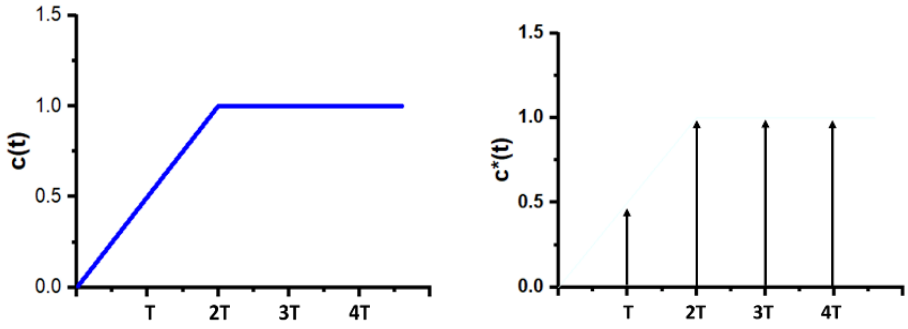

(a) **(b)**

Figure 28. **(a)** Conceptual depiction of a deadbeat response for a continuous-time system subjected to a unit-step input, noting that exact deadbeat performance is unattainable in continuous-time systems [56]; **(b)** Output response of a discrete-time system exhibiting deadbeat behavior for a unit-step input [56].

For a discrete-data system, a deadbeat response at the sampling instants is obtained when the closed-loop transfer function satisfies the following:

$$\frac{C(z)}{R(z)} = \frac{1}{Z^n},$$

which guarantees that the output settles to the reference input in exactly n sampling intervals. The resulting response is of finite duration in the z^{-1} domain. It is important to note that deadbeat response is a property exclusive to discrete-time control systems

and is not attainable in continuous-time frameworks [57].

In this study, the DDC is deployed in all developed models to realize high-speed and precise frequency control in the LFC scheme. The control objective aims to achieve finite-time convergence with negligible oscillatory behavior. Its effectiveness is further evaluated under governor nonlinearities, such as backlash and deadband, which are known to degrade system performance and induce sustained oscillations.

A simplified block diagram of the DDC is presented in **Figure 29**, illustrating its core structure and the corresponding signal flow within the overall load frequency control framework.

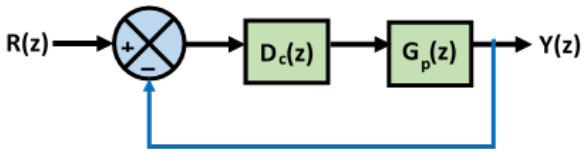

Figure 29. A simple model of a digital controller.

The closed-loop transfer function of the DDC is defined as:

$M(z) = \frac{Y(z)}{R(z)} = z^{-n}$ to achieve a deadbeat response [38], where *n* represents the number of excess poles over zeros in the system. This transfer function implies that the output reproduces the input after exactly (*n*) sampling intervals, thereby ensuring finite-settling-time behavior. Consequently, the closed-loop system exhibits zero steady-state error and eliminates the oscillatory transients commonly associated with conventional feedback controllers. For the present system, the excess pole-zero order is unity (n = 1); hence, the desired deadbeat response is obtained within a single sampling period. The deadbeat characteristic is particularly advantageous for load frequency control applications, as it enables rapid attenuation of frequency deviations and suppression of limit-cycle oscillations induced by nonlinear elements such as governor backlash and deadband.

During signal stabilization, the reference input applied at *R(z)* (as depicted in **Figure 24**) is given by $U \sin \omega_f t$. The corresponding Z-transform of the sampled input signal is [56]:

$$Z[U \sin \omega_f t] = \frac{U z \sin \omega_f T}{z^2 - 2z \cos \omega_f T + 1},$$

where n = 1, the difference of the order of z in the denominator (pole)—the order of z in the numerator (zero) [42].

Hence, $\frac{1}{Z^n} = \frac{1}{Z^1} = z^{-1}$.

Within the SIMULINK framework, this delay is realized using a unit delay block applied to the stabilized output signal. The associated responses verify that the DDC achieves stable, ripple-free, and finite-time settling performance.

3.7.1. Application of DDC in SAPS incorporating a PI controller and a deterministic stabilizing signal

Figure 30a illustrates the block diagram representation of a single-area system with LFC with a deadbeat approach. **Figure 30b** shows the system response of **Figure 30a** and the frequency deviation in a single area LFC with the deadbeat approach.

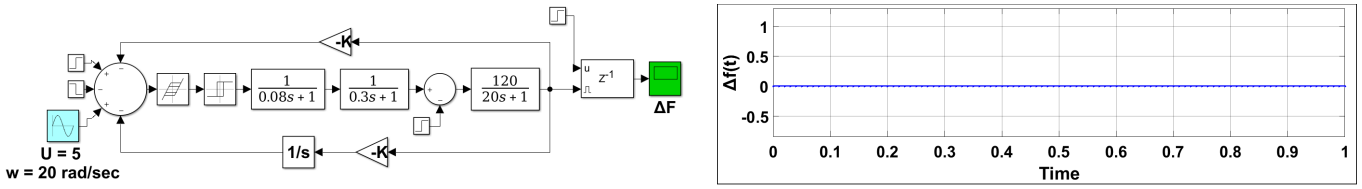

(a) **(b)**

Figure 30. **(a)** Block diagram representation of a single-area system with LFC with the deadbeat approach; **(b)** Frequency deviation in single-area LFC with the deadbeat approach.

3.7.2. Application of DDC in SAPS incorporating an optimal (LQR) controller and a deterministic stabilizing signal

Figure 31a shows the block diagram representation of SAPS with LFC. It uses an LQR controller to maintain frequency stability despite the non-linearity and time constants inherent in the turbine-governor-generator chain. **Figure 31b** shows the dynamic response of the system presented in **Figure 31a** for a single-area LFC using a deadbeat control approach. The deadbeat controller quickly drives the deviation back to zero within a finite time. The response demonstrates fast settling with negligible oscillations. This indicates effective control action and improved system stability.

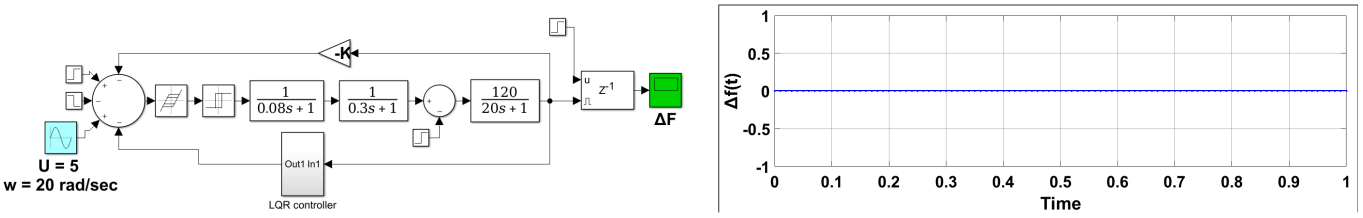

(a) **(b)**

Figure 31. **(a)** Block diagram representation of SAPS with LFC with deadbeat approach and LQR controller; **(b)** Frequency deviation in single-area LFC with deadbeat control approach.

3.7.3. Application of DDC in TwAPS incorporating a PI controller and a deterministic stabilizing signal

Figure 32a shows the Simulink representation with the employment of DDC in TwAPS incorporating a PI controller and a deterministic stabilizing signal. **Figure 32b** represents the results showing the application of DDC in TwAPS in the presence of a PI controller and a deterministic stabilizing signal.

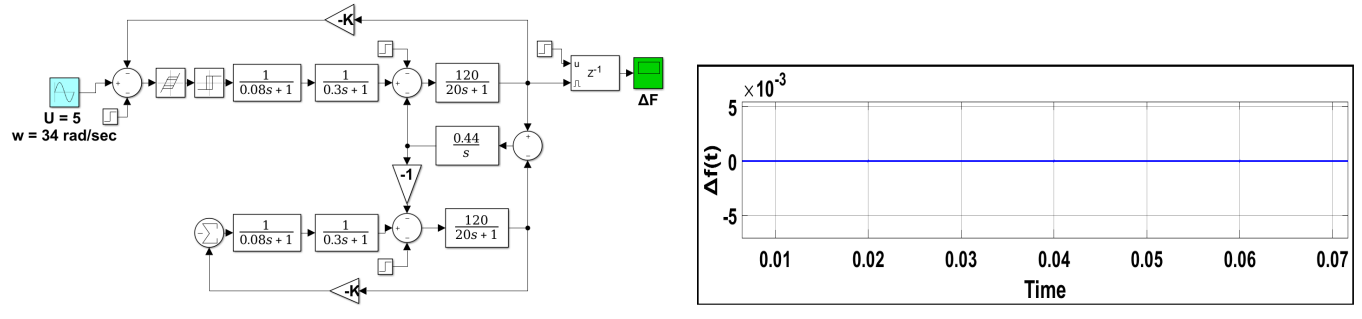

(a) **(b)**

Figure 32. **(a)** Block diagram showing the application of DDC in TwAPS incorporating a PI controller and a deterministic stabilizing signal; **(b)** Results showing the application of DDC in TwAPS in the presence of a PI controller and a deterministic stabilizing signal.

3.7.4. Application of DDC in TwAPS incorporating an optimal (LQR) controller and a deterministic stabilizing signal

Figure 33a represents the Simulink showing the employment of DDC in TwAPS incorporating an optimal (LQR) controller and a deterministic stabilizing signal. **Figure 33b** illustrates the application of DDC in a TwAPS. The system incorporates an optimal controller based on LQR design. The combined control strategy effectively suppresses oscillations and improves dynamic performance. The response demonstrates fast convergence and reduced frequency deviations in both areas.

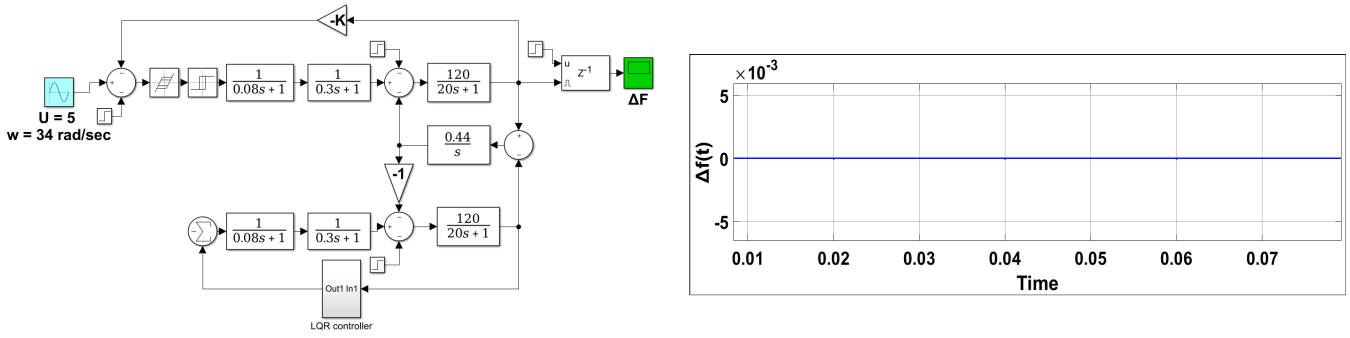

(a) **(b)**

Figure 33. **(a)** Simulink representation showing the employment of DDC in TwAPS incorporating an optimal (LQR) controller and a deterministic stabilizing signal; **(b)** Application of DDC in TwAPS incorporating an optimal (LQR) controller and a deterministic stabilizing signal.

3.7.5. Application of DDC in ThAPS incorporating a PI controller and a deterministic stabilizing signal

Figure 34a shows the Simulink with the employment of DDC in ThAPS incorporating a PI controller and a deterministic stabilizing signal. The system response system response of **Figure 34a** is shown in **Figure 34b,** and the application of DDC in ThAPS incorporating a PI controller and a deterministic stabilizing signal.

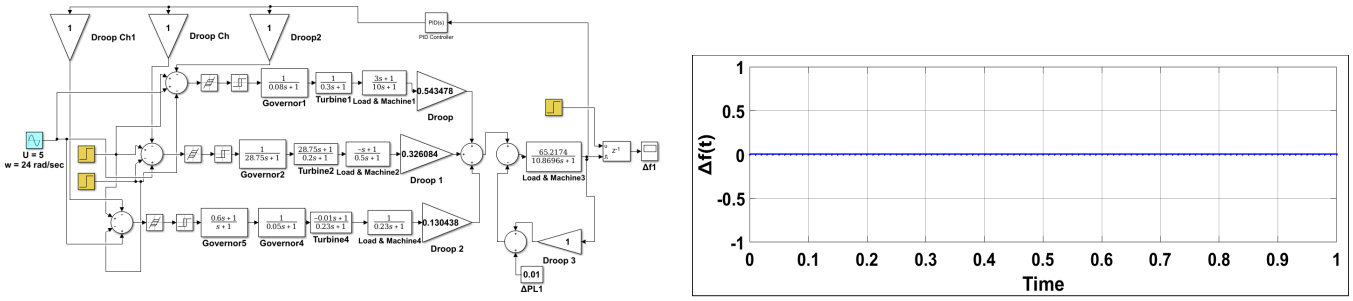

(a) **(b)**

Figure 34. **(a)** Simulink representation showing the employment of DDC in ThAPS incorporating a PI controller and the deterministic stabilizing signal; **(b)** Application of DDC in ThAPS incorporating a PI controller and the deterministic stabilizing signal.

3.7.6. Application of DDC in ThAPS incorporating an optimal (LQR) controller and a deterministic stabilizing signal

Figure 35a shows the Simulink with the employment of DDC in ThAPS incorporating an optimal (LQR) controller and a deterministic stabilizing signal.

Figure 35b illustrates the application of DDC in a ThAPS. The system incorporates an optimal controller designed using the LQR approach. A deterministic stabilizing signal is employed to enhance system performance. The combined control strategy effectively suppresses oscillations and improves dynamic response. The results demonstrate instantaneous achievement of zero frequency deviation with improved stability across all areas.

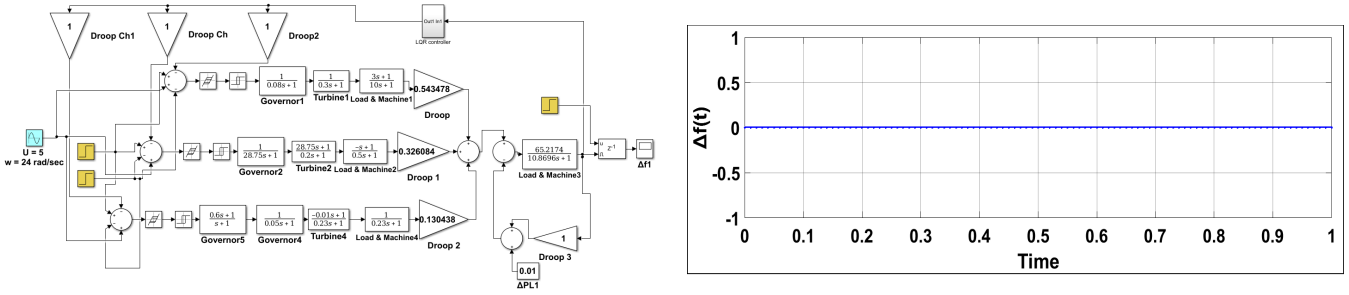

(a) **(b)**

Figure 35. **(a)** Simulink representation showing the employment of DDC in ThAPS incorporating an optimal (LQR) controller and a deterministic stabilizing signal; **(b)** Application of DDC in ThAPS incorporating an optimal (LQR) controller and a deterministic stabilizing signal.

4. The comprehensive results and discussion

Table 1 shows the comprehensive and comparative results of all three models (SAPS, TwAPS, and ThAPS) of LFC using two types of controllers (PI and LQR).

The objective is to propose a method/scheme to achieve zero deviation of frequency ($\Delta f = 0$) at steady state instantly ($t \to 0$) under load changes. All three models with PI controllers fail to yield such expected results, whereas improvement is observed through signal stabilization using Gaussian and deterministic signals. From the perspective of signal stabilization, the presence of high-frequency components is essential for mitigating limit-cycle oscillations. However, the practical realization of an ideal high-pass filter (HPF) is challenging. Therefore, a Gaussian random signal is first generated, and its low-frequency components are attenuated using a low-pass filter (LPF)-based configuration to obtain the desired high-frequency stabilizing signal [58]. In LC suppression using state-feedback pole placement [59], the arbitrary assignment of closed-loop poles requires the system to satisfy the controllability condition. With the LQR controller in SAPS, zero frequency deviation is achieved, but the settling time remains around 5 s; however, with DDC, the settling time reduces to zero as shown in **Figure 31b**. For TwAPS and ThAPS, LQR alone does not satisfy the objective (**Figures 17b** and **25b**), while DDC successfully achieves $\Delta f = 0$ at $t \to 0$ (**Figure 33b**), validating the proposed scheme.

Additionally, the results emphasize the robustness of DDC in handling multi-area system complexities. The integration of deterministic stabilizing signals further enhances control precision and response speed. The proposed scheme ensures superior damping characteristics compared to conventional methods. It also demonstrates scalability across different system configurations without performance degradation. Overall, the approach establishes an effective and reliable solution for instantaneous

frequency regulation in LFC systems.

Table 1. Comprehensive and comparative results of all three models (SAPS, TwAPS, and ThAPS) of LFC using two types of controllers (PI and LQR).

Sl. No.	Models	Controllers used in LFC applications	Performance in LFC					Remarks
			Step response	Estimation of LC	Signal stabilization by deterministic signal	Signal stabilization by Gaussian signal	Application of digital deadbeat	
1	SAPS	PI	**Figure 4b** zero steady-state frequency deviation with a transient lasting up to 16 s.	**Figure 5b** Limit cycle observed at ω = 2.02 rad/s.	**Figure 6b** Synchronized at ω = 20.3 rad/s.	**Figure 7b** stabilization at steady state (t → 0) with Δf = 0.	Steady value Δf = 0 and duration to attain steady state → 0 s. **Figure 30b**	Satisfactory (as anticipated)
2	TwAPS		**Figure 12b** zero steady-state frequency deviation with a transient lasting up to 8 s.	**Figure 13b** Limit cycle observed at ω = 3.4 rad/s.	**Figure 14b** Synchronized at ω = 34.6 rad/s.	**Figure 15b** stabilization at steady state (t → 8).	Steady state Δf = 0, and duration to attain steady state → 0 s. **Figure 32b**	Satisfactory (as anticipated)
3	ThAPS		**Figure 20b** zero steady-state frequency deviation with a transient lasting up to 30 s.	**Figure 21b** Limit cycle observed at ω = 2.38 rad/s.	**Figure 22b** Synchronized at ω = 24.9 rad/s.	**Figure 23b** stabilization at steady state (t → 0) with Δf = 0.7.	Steady state Δf = 0 and duration to attain steady state → 0 s. **Figure 34b**	Satisfactory (as anticipated)
4	SAPS	LQR	**Figure 8b** zero steady-state frequency deviation with a transient lasting up to 15 s.	**Figure 9b** Limit cycle observed at ω = 5 rad/s.	**Figure 10b** Synchronized	**Figure 11b** stabilization at steady state (t → 60) s.	Steady value Δf = 0, and duration to attain steady state → 0 s. **Figure 31b**	Satisfactory (as anticipated)
5	TwAPS		**Figure 16b** zero steady-state frequency deviation with a transient lasting up to 16 s.	**Figure 17b** Limit cycle observed at ω = 1.35 rad/s.	**Figure 18b** Synchronized to ω = 13.1 rad/s.	**Figure 19b** stabilization at steady state (t → 35) with Δf = 15.	Steady state Δf = 0, and duration to attain steady state → 0 s. **Figure 33b**	Satisfactory (as anticipated)
6	ThAPS		**Figure 24b** zero steady-state frequency deviation with a transient lasting up to 15 s.	**Figure 25b** Limit cycle observed at ω = 40 rad/s.	**Figure 26b** Synchronized to ω = 24.9 rad/s.	**Figure 27b** stabilization at steady state (t → 35) with Δf = 1.	Steady state Δf = 0, and duration to attain steady state → 0 s. **Figure 35b**	Satisfactory (as anticipated)

5. Conclusion

As summarized in **Table 1** and illustrated in **Figures 30b**–**35b**, the application of the Digital Deadbeat Controller (DDC) results in the complete mitigation/quenching of limit cycle oscillations for all considered models. The system responses exhibit instantaneous settling (t → 0) with zero frequency deviation (Δf = 0), indicating ideal regulation performance. These results underscore the effectiveness of the proposed method and its potential for real-time implementation in practical power systems.

The final evaluation indicates that the proposed DDC is robust and effective across various LFC models, achieving transient-free operation, negligible ripple, zero steady-state error, and near-instantaneous response. These results demonstrate its applicability to real-time systems and establish a strong foundation for future advancements in power system control methodologies.

Author contributions: KCP has formulated the problem, methodology of analysis adopted, and algorithm of computation presented; AP has validated the results using the SIMULINK toolbox of MATLAB software. All authors have read and agreed to the published version of the manuscript.

Funding: This work received no external funding.

Institutional review board statement: Not applicable.

Informed consent statement: Not applicable.

Data availability statement: No external datasets were used in this study. All relevant data and model parameters necessary to reproduce the results are included within the article.

Acknowledgment: The authors wish to thank the C.V. Raman Global University, Bhubaneswar—752054, Odisha, India, for providing computer facilities for the preparation of this paper.

Conflict of interest: The authors declare no conflict of interest.

AI use statement: During the preparation of this manuscript, the authors used ChatGPT solely for language refinement. No AI tools were used for data analysis, interpretation, or generation of scientific content. All outputs were critically reviewed and edited by the authors. The authors take full responsibility for the integrity and accuracy of the work.

References

1. Jain D, Saxena D. Comprehensive review on control schemes and stability investigation of hybrid AC-DC microgrid. Electric Power Systems Research. 2023; 218: 109182. doi: 10.1016/j.epsr.2023.109182
2. Yang S, Fan X, Zhao Y, et al. A novel method for transient stability margin evaluation of the post-disturbance power system. In: Proceedings of the 15th International Conference on Developments in Power System Protection (DPSP 2020); 9–12 March 2020; Liverpool, UK. doi: 10.1049/cp.2020.0048
3. Dong X, Hao X, Chen Q, et al. A Distributed Power Transfer Limit Calculation Method for Multi-Area Interconnection Power Networks. IEEE Transactions on Power Systems. 2021; 36(5): 4723–4732. doi: 10.1109/TPWRS.2021.3062374
4. Tungadio DH, Sun Y. Load frequency controllers considering renewable energy integration in power system. Energy Reports. 2019; 5: 436–453. doi: 10.1016/j.egyr.2019.04.003
5. Ashfaq T, Mumtaz S, Ahmad S, et al. Automatic Generation Control in Renewables-Integrated Multi-Area Power Systems: A Comparative Control Analysis. Sustainability. 2024; 16(13): 5735. doi: 10.3390/su16135735
6. Fosha C, Elgerd O. The Megawatt-Frequency Control Problem: A New Approach Via Optimal Control Theory. IEEE Transactions on Power Apparatus and Systems. 1970; PAS-89(4): 563–577. doi: 10.1109/TPAS.1970.292603
7. Ali T, Malik SA, Hameed IA, et al. Load Frequency Control and Automatic Voltage Regulation in a Multi-Area Interconnected Power System Using Nature-Inspired Computation-Based Control Methodology. Sustainability. 2022; 14(19): 12162. doi: 10.3390/su141912162
8. Loka R, Parimi AM, Srinivas STP, et al. Region of convergence by parameter sensitivity constrained genetic algorithm-based optimization for coordinated load frequency control in multi-source distributed hybrid power system. Sustainable Energy Technologies and Assessments. 2022; 54: 102887. doi: 10.1016/j.seta.2022.102887
9. Tripathi S, Singh VP, Kishor N, et al. Load frequency control of power system considering electric Vehicles' aggregator with communication delay. International Journal of Electrical Power & Energy Systems. 2023; 145: 108697. doi: 10.1016/j.ijepes.2022.108697
10. Alshammari B, Salah RB, Kahouli O, et al. Design of Fuzzy TS-PDC Controller for Electrical Power System via Rules Reduction Approach. Symmetry. 2020; 12(12): 2068. doi: 10.3390/sym12122068
11. Nguyen BM, Tran-Huynh N, Kawanishi M, et al. Load frequency control design in state space. In: Encyclopedia of Electrical and Electronic Power Engineering. Elsevier; 2023. pp. 314–333. doi: 10.1016/B978-0-12-821204-2.00047-7
12. Shah NN, Pandit AR, Shah MT. Automatic Load Frequency Control of Two Area system Using L-Q-R Method. International Journal Of Current Engineering And Scientific Research. 2016; 3(6): 54–66. Available online: https://troindia.in/journal/ijcesr/vol3iss6/54-66.pdf
13. Kundur P. Power System Stability & Control. Tata McGraw Hill; 2008. pp. 581–626.
14. Saadat H. Power system Analysis. McGraw–Hill Book Company; 1999.
15. Aldeen M, Marsh JF. Decentralised proportional-plus-integral design method for interconnected power systems. IEE Proceedings C Generation, Transmission and Distribution. 1991; 138(4): 263. doi: 10.1049/ip-c.1991.0033
16. Bevrani H, Golpîra H, Messina AR, et al. Power system frequency control: An updated review of current solutions and new challenges. Electric Power Systems Research. 2021; 194: 107114. doi: 10.1016/j.epsr.2021.107114

17. Ahmed M, Magdy G, Khamies M, et al. An efficient coordinated strategy for frequency stability in hybrid power systems with renewables considering interline power flow controller and redox flow battery. Journal of Energy Storage. 2022; 52: 104835. doi: 10.1016/j.est.2022.104835
18. Cavdar B, Sahin E, Sesli E, et al. Cascaded fractional order automatic generation control of a PV-reheat thermal power system under a comprehensive nonlinearity effect and cyber-attack. Electrical Engineering. 2023; 105(6): 4339–4360. doi: 10.1007/s00202-023-01943-y
19. Gulzar MM, Sibtain D, Alqahtani M, et al. Load frequency control progress: A comprehensive review on recent development and challenges of modern power systems. Energy Strategy Reviews. 2025; 57: 101604. doi: 10.1016/j.esr.2024.101604
20. Khan IA, Mokhlis H, Mansor NN, et al. New trends and future directions in load frequency control and flexible power system: A comprehensive review. Alexandria Engineering Journal. 2023; 71: 263–308. doi: 10.1016/j.aej.2023.03.040
21. Tavakoli S, Zamani AA, Khajehoddin A. Efficient load frequency control in multi-source interconnected power systems using an innovative intelligent control framework. Energy Reports. 2024; 11: 2805–2817. doi: 10.1016/j.egyr.2024.02.037
22. Yamashita K, Miyagi H. Multivariable self-tuning regulator for load frequency control system with interaction of voltage on load demand. IEE Proceedings D Control Theory and Applications. 1991; 138(2): 177. doi: 10.1049/ip-d.1991.0025
23. Aldeen M. A Fresh Approach to the LQR Problems with Application to Power Systems. Proceedings of International Conference on Power Engineering; 1993: 374–379.
24. Pan CT, Liaw CM. An adaptive controller for power system load-frequency control. IEEE Transactions on Power Systems. 1989; 4(1): 122–128. doi: 10.1109/59.32469
25. Djukanovic M, Novicevic M, Sobajic DJ, et al. Two-Area Load Frequency Control with Neural Nets. In: Proceedings of the 1993 North American Power Symposium; October 1993; Washington, DC, USA. pp. 161–169.
26. Birch AP. An enhanced neural network load frequency control technique. In: Proceedings of the International Conference on Control '94; 21–24 March 1994; Coventry, UK. pp. 409–415. doi: 10.1049/cp:19940167
27. Li C, Feng C, Li J, et al. Comprehensive frequency regulation control strategy of thermal power generating unit and ESS considering flexible load simultaneously participating in AGC. Journal of Energy Storage. 2023; 58: 106394. doi: 10.1016/j.est.2022.106394
28. Guo W, Wu F. Stability behavior of load adjustment and primary frequency control of pumped storage power plant with upstream and downstream surge tanks. Journal of Energy Storage. 2023; 60: 106626. doi: 10.1016/j.est.2023.106626
29. Yu J, Liao S, Xu J. Frequency control strategy for coordinated energy storage system and flexible load in isolated power system. Energy Reports. 2022; 8: 966–979. doi: 10.1016/j.egyr.2022.02.133
30. Lian Z, Wen C, Guo F, et al. Decentralized secondary control for frequency restoration and power allocation in islanded AC microgrids. International Journal of Electrical Power & Energy Systems. 2023; 148: 108927. doi: 10.1016/j.ijepes.2022.108927
31. Gulzar MM, Iqbal A, Sibtain D, et al. An Innovative Converterless Solar PV Control Strategy for a Grid Connected Hybrid PV/Wind/Fuel-Cell System Coupled With Battery Energy Storage. IEEE Access. 2023; 11: 23245–23259. doi: 10.1109/ACCESS.2023.3252891
32. Perninge M, Eriksson R. Optimal Tertiary Frequency Control in Power Systems with Market-Based Regulation. IFAC-PapersOnLine. 2017; 50(1): 4374–4381. doi: 10.1016/j.ifacol.2017.08.881
33. Carere F, Gatta FM, Geri A, et al. Sardinia as a 100% renewable power system: A frequency stability study. Sustainable Energy, Grids and Networks. 2022; 32: 100899. doi: 10.1016/j.segan.2022.100899
34. Sambariya D, Nath V. Load Frequency Control Using Fuzzy Logic Based Controller for Multi-area Power System. British Journal of Mathematics & Computer Science. 2016; 13(5): 1–19. doi: 10.9734/BJMCS/2016/22899
35. Indulkar CS, Raj B. Application of fuzzy controller to automatic generation control. Electric Machines & Power Systems. 1995; 23(2): 209–220. doi: 10.1080/07313569508955618
36. Chidambaram IA, Velusami S. Decentralized Biased Controllers for Load-Frequency Control of Interconnected Power Systems Considering Governor Dead Band Non-Linearity. In: Proceedings of the 2005 Annual IEEE India Conference—Indicon; 11–13 December 2005; Chennai, India. pp. 521–525. doi: 10.1109/INDCON.2005.1590225
37. Patra KC, Kar N, Patnaik A. Suppression Limit Cycles in 2x2 Nonlinear Systems with Memory Type Nonlinearities. Design, Construction, Maintenance. 2024; 4: 169–185. Doi: 10.37394/232022.2024.4.18

38. Patra KC, Patnaik A. Load Frequency Control by Speed Governors of Two-Area Power System using Digital Controller with Deadbeat Approach. International Journal of Electrical Engineering and Computer Science. 2025; 7: 200–217. doi: 10.37394/232027.2025.7.19
39. Parmar KPS, Majhi S, Kothari DP. Automatic generation control of an interconnected hydrothermal power system. In: Proceedings of the 2010 Annual IEEE India Conference (INDICON); 17–19 December 2010; Kolkata, India. pp. 1–5. doi: 10.1109/INDCON.2010.5712663
40. Kothari DP, Nagrath IJ. Modern Power System Analysis. McGraw-Hill; 2003.
41. Elgerd OI. Electric Energy Systems Theory: An Introduction. Tata McGraw-Hill; 1983.
42. Stefani RT, Shahian B, Savant CJ, et al. Design of Feedback Control Systems. Oxford University Press; 2002.
43. Llewis FL, Syrmos VL. Optimal Control. John Wiley & Sons; 1995.
44. Azzam M. Robust automatic generation control. Energy Conversion and Management. 1999; 40(13): 1413–1421. doi: 10.1016/S0196-8904(99)00040-0
45. Sivanagaraju S, Sreenivasan G. Power System Operation and Control. Pearson Education India; 2009.
46. Kakilli A, Oguz Y, Çalik, H. The Modelling of Electric Power Systems on the State Space and Controlling of Optimal LQR Load Frequency. Journal of Electrical & Electronics Engineering. 2009; 9(2). Available online: https://electricajournal.org/public/pdfs/63/6.pdf
47. Patra KC, Patnaik A. Estimation of Limit Cycles and Signal Stabilization with Deadbeat approach in three Dimensional Nonlinear systems. International Journal of Control Systems and Robotics. 2025; 10: 22–38.
48. Patra KC, Patnaik A. Investigation of Limit Cycles and Signal Stabilization by Deterministic and Gaussian Random Signals Based on Deadbeat Approach in 3×3 Nonlinear Systems with Memory Nonlinearities. International Journal of Electrical Engineering and Computer Science. 2025; 7: 159–188. doi: 10.37394/232027.2025.7.17
49. Patra KC, Kar N. Suppression limit cycles in 2 × 2 nonlinear systems with memory type nonlinearities. International Journal of Dynamics and Control. 2022; 10(3): 721–733. doi: 10.1007/s40435-021-00860-x
50. Oldenburger R, Nakada T. Signal stabilization of self-oscillating systems. IRE Transactions on Automatic Control. 1961; 6(3): 319–325. doi: 10.1109/TAC.1961.1105218
51. Gelb A, Velde WEV. Multiple-Input describing functions and nonlinear system design. In: BiblioBoard Library Catalog. McGraw-Hill; 1968.
52. Atherton DP, Towill DR. Nonlinear Control Engineering-Describing Function Analysis and Design. IEEE Transactions on Systems, Man, and Cybernetics. 1977; 7(9): 678–678. doi: 10.1109/TSMC.1977.4309808
53. Tsay TS. Load–frequency control of interconnected power system with governor backlash nonlinearities. International Journal of Electrical Power & Energy Systems. 2011; 33(9): 1542–1549. doi: 10.1016/j.ijepes.2011.06.005
54. Sah SV, Prakash V, Pathak PK, et al. Fractional Order AGC Design for Power Systems via Artificial Gorilla Troops Optimizer. In: Proceedings of the 2022 IEEE International Conference on Power Electronics, Drives and Energy Systems (PEDES); 14–17 December 2022; Jaipur, India. pp. 1–6. doi: 10.1109/PEDES56012.2022.10079975
55. Hussain J, Zou R, Wu Z, et al. Design and Performance Analysis of Walrus Optimization Algorithm (WaOA)—Based Cascade Controller for Load Frequency Control of a Multi-Area Power System With Renewable Sources. International Journal of Numerical Modelling: Electronic Networks, Devices and Fields. 2025; 38(2): e70046. doi: 10.1002/jnm.70046
56. Kuo BC. Digital Control Systems. Oxford University Press; 2009.
57. Ogata K. Discrete-Time Control Systems. Prentice-Hall; 2009.
58. Taub H, Schilling DL, Saha G. Principles of Communication Systems. Tata McGraw-Hill; 2008. p. 107.
59. Wang C, Yang M, Zheng W, et al. Analysis and Suppression of Limit Cycle Oscillation for Transmission System With Backlash Nonlinearity. IEEE Transactions on Industrial Electronics. 2017; 64(12): 9261–9270. doi: 10.1109/TIE.2017.2711564